PHYSICAL REVIEW B **105**, 214526 (2022)

Superconductivity and phase diagrams of CaK$(Fe_{1-x}Mn_x)_4As_4$ single crystals

M. Xu,[1,2] J. Schmidt,[1,2] E. Gati,[1,2,3] L. Xiang,[1,2,4] W. R. Meier,[1,2,5] V. G. Kogan,[1] S. L. Bud'ko,[1,2] and P. C. Canfield[1,2,*]
[1]*Ames Laboratory, Iowa State University, Ames, Iowa 50011, USA*
[2]*Department of Physics and Astronomy, Iowa State University, Ames, Iowa 50011, USA*
[3]*Max Planck Institute for Chemical Physics of Solids, 01187 Dresden, Germany*
[4]*National High Magnetic Field Laboratory, Florida State University, Tallahassee, Florida 32310, USA*
[5]*Department of Materials Science and Engineering, University of Tennessee Knoxville, Knoxville, Tennessee 37996, USA*

(Received 22 April 2022; revised 8 June 2022; accepted 17 June 2022; published 28 June 2022)

In order to study the effects of Mn substitution on the superconducting and magnetic ground state of $CaKFe_4As_4$ ($T_c = 35$ K), members of the CaK$(Fe_{1-x}Mn_x)_4As_4$ series have been synthesized by high-temperature solution growth in single-crystalline form and characterized by elemental analysis, thermodynamic, and transport measurements. These measurements show that the superconducting transition temperature decreases monotonically and is finally suppressed below 1.8 K as x is increased from 0 to 0.036. For x values greater than 0.016, signatures of a magnetic transition can be detected in both thermodynamic and transport measurements in which kinklike features allow for the determination of the transition temperature T^* that increases as Mn substitution increases. A temperature-composition (T-x) phase diagram is constructed, revealing a half-dome of superconductivity with the magnetic transition temperature T^* appearing near 26 K for $x \sim 0.017$ and rising slowly up to 33 K for $x \sim 0.036$. In addition to the creation of the T-x phase diagram for CaK$(Fe_{1-x}Mn_x)_4As_4$, specific-heat data are used to track the jump in specific heat at T_c; the CaK$(Fe_{1-x}Mn_x)_4As_4$ data do not follow the scaling of ΔC_p with T_c^3 as many of the other Fe-based superconducting systems do. These data suggest that, as magnetic pair breaking is present, the jump in C_p for a given T_c is reduced. Elastoresistivity coefficients $2m_{66}$ and $m_{11} - m_{12}$ as a function of temperature are also measured. $2m_{66}$ and $m_{11} - m_{12}$ are qualitatively similar to CaK$(Fe_{1-x}Ni_x)_4As_4$. This may indicate that the magnetic order in Mn-substituted system may be still the same as CaK$(Fe_{1-x}Ni_x)_4As_4$. Superconductivity of CaK$(Fe_{1-x}Mn_x)_4As_4$ is also studied as a function of magnetic field. A clear change in $H'_{c2}(T)/T_c$, where $H'_{c2}(T)$ is $dH_{c2}(T)/dT$, at $x \sim 0.015$ is observed and probably is related to change of the Fermi surface due to magnetic order. Coherence lengths and the London penetration depths are also calculated based on H_{c1} and H_{c2} data. Coherence lengths as the function of x also show the changes near $x = 0.015$, again consistent with Fermi-surface changes associated with the magnetic ordering seen for higher-x values.

DOI: 10.1103/PhysRevB.105.214526

I. INTRODUCTION

Since their discovery in 2008 [1], the study of Fe-based superconductors has led to extensive experimental interest and their variety offers the opportunity of understanding unconventional superconductivity in a broader sense. Although diverse, several families of Fe-based superconductors share similar crystal structures [2–4] all featuring edge-shared tetrahedral Fe-As or Fe-Se layers, and phase diagrams [2–18] that suggest a relationship between, or proximity of, superconducting and magnetic and/or nematic ordering or fluctuations. The role of magnetic as well as structural transitions and fluctuations in unconventional superconductivity is still an open topic, attracting both theoretical and experimental research. The relationship between these states is believed to be key to understanding unconventional superconductivity [19].

Within the Fe-based superconductors, three structural classes, $AeFe_2As_2$ ($Ae =$ alkaline earth) (122) families [2–9], $AeAFe_4As_4$ ($A =$ alkaline metal) (1144) family [10–13,16,17], and FeSe [14,15] provide a microcosm of many of the key questions at hand. At ambient pressure, doped 122 systems manifest the most common interplay between stripelike antiferromagnetic order, nematicity, and superconductivity [3,8]. On the other hand, the Ni-substituted 1144 system has hedgehog-spin-vortex-crystal (h-SVC)–type antiferromagnetic (AFM) order and superconductivity interacting with each other without any structural phase transition [13,20]. In contrast, at ambient pressure, FeSe has a nematiclike transition and superconductivity, but no magnetic order [14,15]. The comparison of these three classes of Fe-based superconductors allows us to examine the effects of the presence or absence of nematicity and magnetic order on the superconducting state. In related 1144 systems, such as $EuRbFe_4As_4$, the presence of a lattice of moment bearing Eu^{2+} gives rise to more complex magnetic ordering [21,22].

$CaKFe_4As_4$ is a structurally ordered, quaternary compound that intrinsically superconducts with T_c around 35 K [10,11]. As such, it offers the possibility of studying the effects of Mn substitution on the superconducting state [23,24]. Given

---

[*] canfield@ameslab.gov

that it was not possible to induce superconductivity in the $\mathrm{Ba(Fe_{1-x}Mn_x)_2As_2}$ system [25,26], one of the motivations for this study was to gain insight into how Mn affects superconductivity in the $\mathrm{CaK(Fe_{1-x}Mn_x)_4As_4}$ system. This is of particular interest given the fact that Mn, of all the $3d$ transition metals, is most likely to manifest local-moment-like properties akin to what can be found for rare earths such as Gd.

A second motivation for this study of the $\mathrm{CaK(Fe_{1-x}Mn_x)_4As_4}$ system is based on the similarities between $\mathrm{CaKFe_4As_4}$ and $\mathrm{Ba_{0.5}K_{0.5}Fe_2As_2}$, both having the same nominal electron count and presenting only a superconducting transition upon cooling. This analogy was explored [13] in the study of the similarities between the underdoped ($x < 0.5$) $\mathrm{Ba_{1-x}K_xFe_2As_2}$ and Ni/Co-doped $\mathrm{CaKFe_4As_4}$ phase diagrams, both showing a $\frac{1}{2}$ dome of superconductivity with increasing AFM ordering (T_N) coinciding with decreasing superconducting T_c. Study of $\mathrm{CaK(Fe_{1-x}Mn_x)_4As_4}$ allows us to investigate to what extent this analogy between the K-doped 122 and transition-metal-doped 1144 phase diagrams holds. In particular, we compare nominally hole-doped $\mathrm{CaK(Fe_{1-x}Mn_x)_4As_4}$ with overdoped ($x > 0.5$) $\mathrm{Ba_{1-x}K_xFe_2As_2}$. Even though superconductivity is suppressed in both cases, we found a fundamental difference between the two phase diagrams: a magnetic phase transition line appears in the $\mathrm{CaK(Fe_{1-x}Mn_x)_4As_4}$ compounds upon doping, which is not present for overdoped $\mathrm{Ba_{1-x}K_xFe_2As_2}$. In addition, at a quantitative level, Mn substitution suppresses T_c much more rapidly than what was found for Co or Ni substitution.

In this paper, we detail the synthesis and characterization of $\mathrm{CaK(Fe_{1-x}Mn_x)_4As_4}$ single crystals. A temperature-composition (T-x) phase diagram is constructed by elemental analysis, thermodynamic, and transport measurements. In addition to creating the T-x phase diagram, specific heat and elastoresistivity are also measured to track the jump in specific heat at T_c and investigate the evolution of nematic fluctuations. Coherence lengths and the London penetration depths are also calculated based on H_{c1} and H_{c2} data obtained from measurements. Finally, temperature vs change of electron count, $|\Delta e^-|$, phase diagram of $\mathrm{CaK(Fe_{1-x}TM_x)_4As_4}$ single crystals (TM = Mn, Ni and Co) is also presented and discussed.

II. CRYSTAL GROWTH AND EXPERIMENTAL METHOD

Single-crystalline $\mathrm{CaK(Fe_{1-x}Mn_x)_4As_4}$ samples were grown by high-temperature solution growth [27] out of FeAs flux in the manner similar to pure $\mathrm{CaKFe_4As_4}$ [11,12]. Lumps of potassium metal (Alfa Aesar 99.95%), distilled calcium metal pieces [Ames Laboratory, Materials Preparation Center (MPC 99.9%)], and $\mathrm{Fe_{0.512}As_{0.488}}$ and $\mathrm{Mn_{0.512}As_{0.488}}$ precursor powders were loaded into a 1.7-ml fritted alumina Canfield Crucible Set [28] (LSP Industrial Ceramics, Inc.) in an argon-filled glove box. The ratio of K:Ca:$\mathrm{Fe_{0.512}As_{0.488}}$ and $\mathrm{Mn_{0.512}As_{0.488}}$ was 1.2:0.8:20. A 1.3-cm outer diameter and 6.4-cm-long tantalum tube which was used to protect the silica ampoule from reactive vapors was welded with the crucible set in partial argon atmosphere inside. The sealed Ta tube was then itself sealed into a silica ampoule and the ampoule was placed inside a box furnace. The furnace was held for 2 h at 650 °C before increasing to 1180 °C and held there for 5 h to make sure the precursor was fully melted. The furnace was then fast cooled from 1180 °C to 960 °C in 1.5 h. Crystals were grown during a slow cooldown from 960 °C to 920 °C over 48 h. After 1–2 h at 920 °C, the ampoule was inverted into a centrifuge and spun to separate the remaining liquid from the grown crystals. Metallic, platelike, crystals were obtained but, unfortunately, with both average size and thickness diminishing by a factor 2–4 as x is increased.

Similar to $\mathrm{CaKFe_4As_4}$ [12], single crystals of $\mathrm{CaK(Fe_{1-x}Mn_x)_4As_4}$ are soft and malleable which makes them difficult to grind for powder x-ray diffraction measurements. Diffraction measurements were carried out on single-crystal samples, which were cleaved along the (001) plane, using a Rigaku MiniFlex II powder diffactometer in Bragg-Brentano geometry with Cu $K\alpha$ radiation ($\lambda = 1.5406$ Å) [29].

The Mn-substitution levels (x) of the $\mathrm{CaK(Fe_{1-x}Mn_x)_4As_4}$ crystals were determined by energy-dispersive spectroscopy (EDS) quantitative chemical analysis using an EDS detector (Thermo NORAN Microanalysis System, model C10001) attached to a JEOL scanning-electron microscope (SEM). The compositions of platelike crystals were measured at three separate positions on each crystal's face (parallel to the crystallographic *ab* plane) after cleaving them. An acceleration voltage of 16 kV, working distance of 10 mm, and takeoff angle of 35° were used for measuring all standards and crystals with unknown composition. Pure $\mathrm{CaKFe_4As_4}$ was used as a standard for Ca, K, Fe, and As quantification. $\mathrm{SmMn_2Ge_2}$ and $\mathrm{GdMn_2Ge_2}$ were used as standards for Mn, both leading to consistent results without significant difference within the experimental error (~0.0015). The spectra were fitted using NIST-DTSA II Lorentz 2020-06-26 software [30]. Different measurements on the same sample reveal good homogeneity in each crystal and the average compositions and error bars were obtained from these data, accounting for both inhomogeneity and goodness of fit of each spectra.

Temperature and magnetic field-dependent magnetization and resistance measurements as well as temperature-dependent specific-heat measurements were carried out by using Quantum Design (QD), Magnetic Property Measurement Systems (MPMS). and Physical Property Measurement Systems (PPMS). Field-dependent magnetization data from which H_{c1} is obtained was collected by Quantum Design MPMS-3 using quartz sample holder with magnetic field parallel to the crystallographic *ab* plane. Temperature-dependent magnetization measurements were taken for $H \parallel ab$ by placing the platelike sample between two collapsed plastic straws with the third, uncollapsed, straw providing support as a sheath on the outside. The single-crystal samples of $\mathrm{CaK(Fe_{1-x}Mn_x)_4As_4}$ measured in the MPMS have platelike morphology with length and width from 3 to 10 mm and thickness (c axis) 50–200 μm. The approximate effective demagnetizing factor N ranges from 0.007 to 0.077 with magnetic field applied parallel to the crystallographic *ab* plane [31]. Since the value of N is small, we neglect the demagnetizing field when magnetic field was applied parallel to the crystallographic *ab* plane. AC electrical resistance measurements were performed in a standard four-contact geometry using the ACT option of the PPMS, with a 3-mA excitation and a frequency of 17 Hz. 50-μm diameter Pt wires were bonded to the samples with silver paint (DuPont 4929N) with contact resistance values of about 2–3 Ohms. The magnetic field, up to 90 kOe, was applied along *c* or *ab* directions, with the current flowing in the *ab* plane. Temperature-dependent specific-heat measurements were carried out by using the relaxation technique as implemented in the heat capacity option of the PPMS. Due to small masses of the individual crystals for some concentrations, stacks of several crystals were used when needed, with thin layers of Apiezon N grease in-between.

Elastoresistance measurements were performed using a technique similar to that described in Refs. [32,33]. To this end, samples of $\mathrm{CaK(Fe_{1-x}Mn_x)_4As_4}$ were cleaved and cut into barlike shapes of dimensions $\approx 1.5\times 0.3\times 0.02\ \mathrm{mm}^3$. The orientation of the long side of the crystals was chosen to be either the $[1\ 1\ 0]_T$ or the $[1\ 0\ 0]_T$ direction (the notion $[...]_T$ refers to the tetragonal unit cell). For each direction, two crystals were glued orthogonally on a piezoelectric actuator from Piezomechanik using Devcon 5-Minute Epoxy. In previous works [32], it was demonstrated that this glue provides a strain transmission of ≈80% below 250 K. Strictly speaking, samples glued on the piezoelectric actuator experience biaxial strain upon application of a voltage. However, the biaxial strain is highly anisotropic, i.e., has opposite signs in the two orthogonal directions. Thus, we denote the strain along the poling directions of the actuator as ϵ_{xx}, and the strain perpendicular to it as ϵ_{yy}. Correspondingly, we denote the resistance of the sample, whose long axis is parallel to ϵ_{xx} (ϵ_{yy}), as R_{xx} (R_{yy}). The resistances R_{xx} and R_{yy} were measured in a standard four-point configuration with LakeShore's resistance bridges LS370 and LS372, with contacts made by spot welding 25-μm diameter Pt wires to the sample resulting in contact resistances of typically 1 Ω. The strains ϵ_{xx} and ϵ_{yy}, created by the application of voltages between −30 and 120 V to the actuator, were measured by two orthogonal strain gauges that were placed on the surface of the actuator opposite to the one on which samples were attached. The low-temperature environment was provided by a Janis SHI-950T-X closed cycle refrigerator, with the sample in ^{4}He exchange gas.

III. $\mathrm{CaK(Fe_{1-x}Mn_x)_4As_4}$ STRUCTURE AND COMPOSITION

Figure 1 presents single-crystal diffraction data of $\mathrm{CaK(Fe_{1-x}Mn_x)_4As_4}$ with $x_{\mathrm{EDS}} = 0.036$. From the figure, we can see that all $(00l)$, $l \leqslant 12$, are detected. The $h + k + l =$ odd peaks which are forbidden for the $I4/\mathrm{mmm}$ structure [10] can be clearly found. This indicates that sample has the anticipated $P4/\mathrm{mmm}$ structure associated with the $\mathrm{CaKFe_4As_4}$ structure [10,11,13].

The Mn substitution x_{EDS}, determined by EDS, is shown in Fig. 2 for different crystals as a function of the nominal Mn fraction x_{nominal} that was originally used for the growth. Error bars account for both possible inhomogeneity of substitution and goodness of fit of each EDS spectra. A clear correlation can be seen between the nominal and the measured substitution levels, with a proportionality factor of 0.60 ± 0.01. From this point onward, x_{EDS} will be used when referring to Mn-substitution level. For comparison, the ratio of measured to nominal Ni and Co fraction in the corresponding $\mathrm{CaK(Fe_{1-x}\mathit{TM}_x)_4As_4}$ are 0.64 and 0.79, respectively [13].

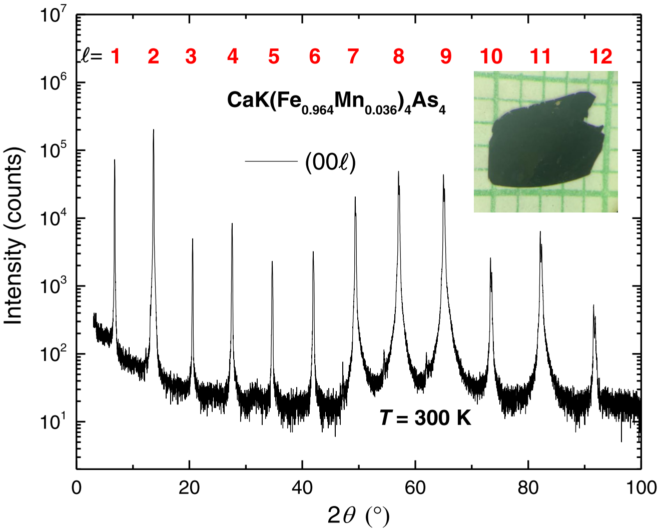

FIG. 1. X-ray diffraction data showing $(00l)$ diffraction peaks from in-laboratory diffraction measurements on a single-crystalline plate plotted on a semilog scale. The value of l is shown in red above each peak. Note that l = odd $(00l)$ lines are evidence of the ordered $\mathrm{CaKFe_4As_4}$ structure [10,11]. Inset picture shows a $\mathrm{CaK(Fe_{1-x}Mn_x)_4As_4}$ single-crystalline plate over a millimeter grid.

IV. DATA ANALYSIS AND PHASE DIAGRAM

Figure 3 shows the low-temperature (1.8–45 K), zero-field-cooled-warming (ZFCW) magnetization for $\mathrm{CaK(Fe_{1-x}Mn_x)_4As_4}$ single crystals for $H_{\parallel ab} = 50$ Oe [field-cooled-warming (FCW) and ZFCW magnetization data for an $x = 0.016$ sample can be found in Fig. 21 in the Appendix]. M is the volumetric magnetic moment in this

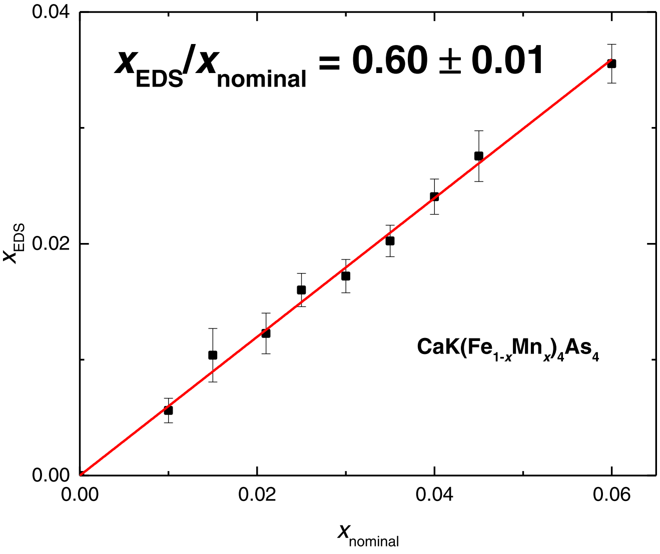

FIG. 2. EDS measured Mn concentration vs nominal Mn concentration for the $\mathrm{CaK(Fe_{1-x}Mn_x)_4As_4}$ series. The line is the linear fit of data with fixing intercept to 0.

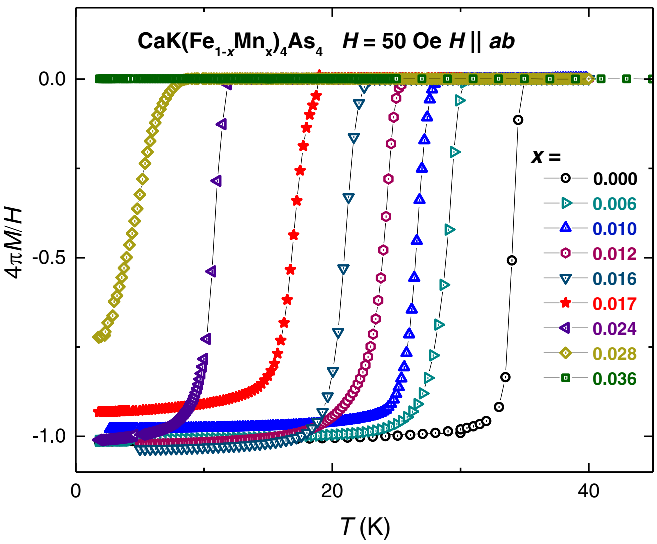

FIG. 3. Zero-field-cooled-warming (ZFCW) low-temperature magnetization as a function of temperature for CaK(Fe$_{1-x}$Mn$_x$)$_4$As$_4$ single crystals with a field of 50 Oe applied parallel to the crystallographic *ab* plane. *M* is the volumetric magnetic moment with cgs unit emu cm^{-3} or Oe.

figure and is calculated by using the density of CaKFe$_4$As$_4$, which is determined to be 5.22 g/cm^3 from lattice parameters at room temperature [10]. A magnetic field of 50 Oe was applied parallel to the *ab* plane (i.e., parallel to the surface of the platelike crystal). The superconducting transitions (T_c) are clearly seen in this graph except for the highest substitution value $x = 0.036$. As the value of the Mn substitution x increases, the superconducting transition temperature decreases. For $x = 0.028$, a full magnetic shielding is not reached by 1.8 K.

TABLE I. Table shows effective μ_{eff} Curie-Weiss temperature θ, temperature-independent susceptibility χ_0 obtained from Curie-Weiss fit to the difference magnetization ($\Delta M'$) between CaKFe$_4$As$_4$ and CaK(Fe$_{1-x}$Mn$_x$)$_4$As$_4$ single crystals as a function of temperature from 40 to 150 K for a field of 10 kOe applied parallel to the crystallographic *ab* plane. The θ values were fixed to the inferred values of T^* or their extrapolated values (see text for details).

x_{EDS}	μ_{eff}, μ_B	θ (K)	χ_0 ($\frac{\text{emu}}{\text{mol Oe}}$)	R^2(COD)
0.006	5.47 (0.18)	22.0	-0.0132	0.9977
0.010	4.26 (0.22)	23.9	-0.0021	0.9985
0.012	4.82 (0.14)	24.6	-0.0021	0.9985
0.016	4.55 (0.09)	25.5	-0.0010	0.9948
0.017	4.69 (0.08)	26.5	-0.0060	0.9975
0.024	5.18 (0.07)	28.8	-0.0042	0.9986
0.028	4.63 (0.08)	30.0	-0.0046	0.9911
0.036	4.93 (0.05)	35.5	-0.0065	0.9954

Figure 4 shows the low-temperature (5–100 K) $M(T)/H$ data for CaK(Fe$_{1-x}$Mn$_x$)$_4$As$_4$ single crystals with 10-kOe field applied parallel to the crystallographic *ab* plane. There is an appearance of a Curie-Weiss tail after adding Mn and kinklike features found around 30 K for $x > 0.010$, which may indicate new phase transition (T^*). The inset shows $M(T)/H$ of a CaK(Fe$_{0.976}$Mn$_{0.024}$)$_4$As$_4$ single crystal over a wider temperature range. As Mn is added, the Curie-tail-like feature grows. Although the Mn doping levels are low ($x < 0.05$), the $M(T)$ data can be fit by a $C/(T+\theta) + \chi_0$ function when we take θ to be equal to T^*, or its extrapolation by linear fitting T^* from Fig. 7 to $x = 0.006$ for low x, where T^* is absent (see Table I in the Appendix). The effective moment calculated per Mn is found to be ∼5 μB. This means that the substitution of Mn brings more local-moment-like behavior to this system.

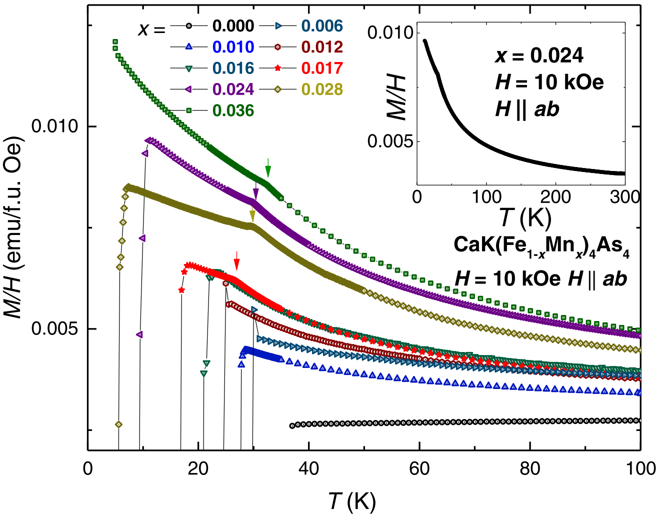

FIG. 4. Low-temperature magnetization divided by applied field as a function of temperature for CaK(Fe$_{1-x}$Mn$_x$)$_4$As$_4$ single crystals with a field of 10 kOe applied parallel to the crystallographic *ab* plane. The inset shows the CaK(Fe$_{0.976}$Mn$_{0.024}$)$_4$As$_4$ single-crystal magnetization for 5 K $< T <$ 300 K. Small vertical arrows indicate the location of T^* (see Appendix for criterion).

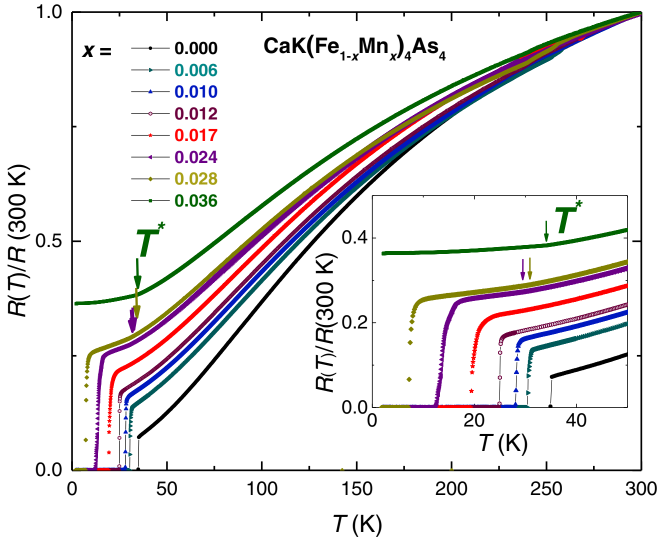

FIG. 5. Temperature dependence of normalized resistance $R(T)/R$(300 K) of CaK(Fe$_{1-x}$Mn$_x$)$_4$As$_4$ single crystals showing the suppression of the superconducting transition T_c and the appearance and evolution of a kinklike feature, marked with arrows. The criterion used to determine T^* from this kink feature is outlined and discussed in the Appendix.

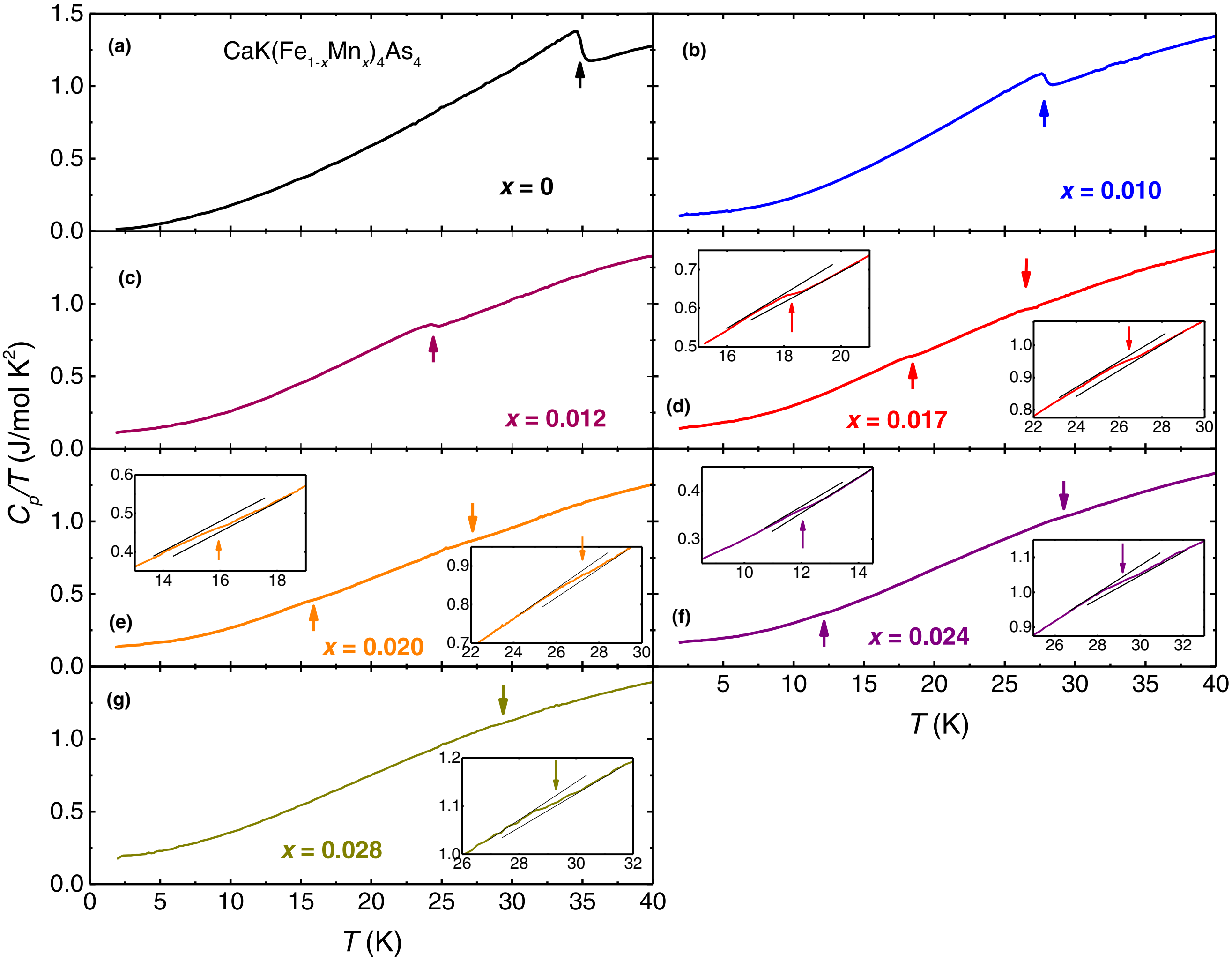

FIG. 6. Heat capacity of CaK$(Fe_{1-x}Mn_x)_4As_4$ single crystals, and criteria used to determine T^* and T_c, show transition temperatures of T_c (upward arrows) and T^* (downward arrows) for different substitution levels: $x = 0.000$ (a), $x = 0.010$ (b), $x = 0.012$ (c), $x = 0.017$ (d), $x = 0.020$ (e), $x = 0.024$ (f) and $x = 0.028$ (g).

For $x > 0.016$, a kinklike feature can be seen at a temperature T^*. As x increases from 0.016 to 0.036, the temperature T^* increases from ~30 to ~35 K. The criterion for determining T^* is shown in Fig. 22 in the Appendix.

Figure 5 presents the temperature-dependent, normalized, electrical resistance of CaK$(Fe_{1-x}Mn_x)_4As_4$ single crystals. RRR [the ratio of R(300 K) and resistance before T_c] decreases as Mn substitution increases, which indicates disorder increasing. [See Fig. 19 in the Appendix for $R(40\ K)/R(300\ K)$ as a function of x as well as the directly measured $\rho(40\ K)$ for selected x values.] The superconducting transition temperatures decrease as Mn is added to the system. When $x = 0.036$, there is no signature of a superconducting transition detectable above 1.8 K. With increasing Mn content, a kink appears for $x > 0.017$ and rises to about 33 K for $x = 0.036$. A similar feature also appeared in Ni- and Co-substituted $CaKFe_4As_4$ and $RbEuFe_4As_4$ electrical resistance measurements [13,34,35]. The criterion for determining the transition temperature T^* associated with this kink is shown in Fig. 22(c).

Figure 6 presents the temperature-dependent specific-heat data divided by temperature for $T < 45$ K. Whereas the feature associated with superconductivity (centered around T_c) is relatively clear (marked by upward pointing arrows), at least for lower-x values, the feature associated with T^* (marked by downward pointing arrows) is quite subtle and is shown more clearly in the insets. Transition temperature is inferred from the midpoint of the feature. As has been already seen in the magnetization as well as resistance data, the addition of Mn (increase of x value) leads to a suppression of T_c as well as an onset and gradual increase of T^* above a threshold value of $x \sim 0.017$.

Figure 7 summarizes the transition temperature results inferred from magnetization, resistance, and specific-heat measurements, plotting the superconducting and magnetic transitions as a function of substitution, constructing the T-x phase diagram for the CaK$(Fe_{1-x}Mn_x)_4As_4$ system. As depicted in this phase diagram, increasing Mn substitution (i) suppresses T_c monotonically with it extrapolating to 0 K by $x \lesssim 0.036$ and (ii) stabilizes a new transition,

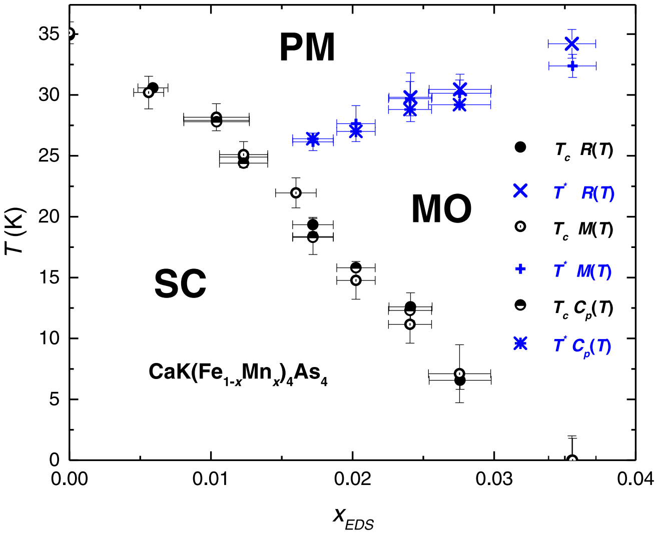

FIG. 7. Temperature-composition phase diagram of $CaK(Fe_{1-x}Mn_x)_4As_4$ single crystals as determined from resistance [$R(T)$], magnetization [$M(T)$], and specific-heat [$C_p(T)$] measurements. The circular symbols denote the T_c phase line and the crosslike symbols denote the T^* phase line, most likely associated with antiferromagnetic order. Superconducting (SC), magnetically ordered (MO), and paramagnetic (PM) regions are denoted. Details of how the MO line extends into the SC state are not addressed in this phase diagram.

presumably an antiferromagnetic one, for $x \gtrsim 0.016$ with the transition temperature rising from $\sim$26 K for $x = 0.017$ to $\sim$33 K for $x = 0.036$. Each phase line is made out of data points inferred from $R(T)$, $M(T)$, and $C_p(T)$ measurements, illustrating the good agreement between our criterion for inferring T_c and T^*. The $CaK(Fe_{1-x}Co_x)_4As_4$ and $CaK(Fe_{1-x}Ni_x)_4As_4$ series have qualitatively similar phase diagrams, with the quantitative differences being associated with the doping levels necessary to induce the magnetic phase and to suppress superconductivity. Further comparisons of the $CaK(Fe_{1-x}Mn_x)_4As_4$ phase diagram to the phase diagrams of the $CaK(Fe_{1-x}Co_x)_4As_4$ and $CaK(Fe_{1-x}Ni_x)_4As_4$ series, as well as doped $BaFe_2As_2$ series, will be made in the Discussion section below.

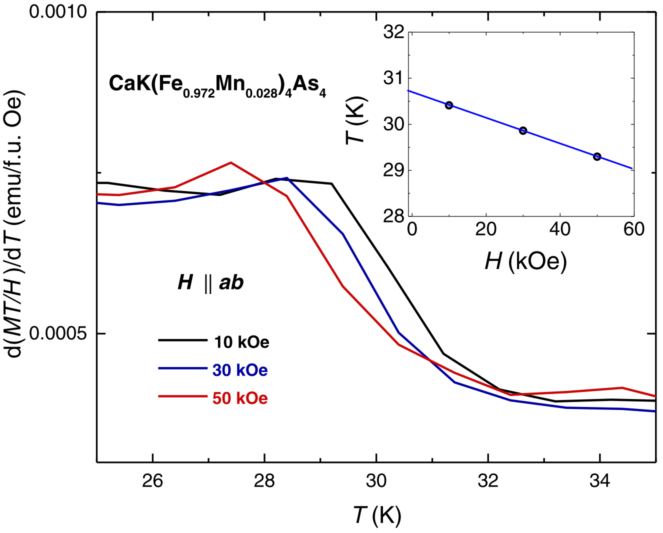

FIG. 8. $d(MT/H)/dT$ vs T of $CaK(Fe_{0.972}Mn_{0.028})_4As_4$ single crystal with 10, 30, and 50 kOe applied parallel to the crystallographic ab plane. Inset shows transition temperature T^*, inferred for different applied field values using the same criterion shown in the Appendix. The solid blue line is linear fit to the data points, extrapolating to 30.7 K for $H = 0$.

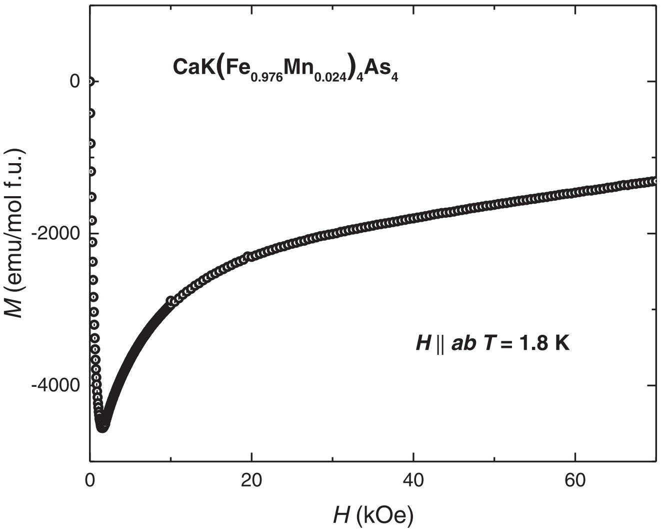

FIG. 9. Magnetization of a single crystal of $CaK(Fe_{0.976}Mn_{0.024})_4As_4$ as a function of magnetic field applied parallel to the crystallographic ab plane at 1.8 K. Temperature is ZFC to 1.8 K and demagnetization is done at 60 K before cooling to minimize the remnant magnetic field.

Given that the $R(T)$ and $C_p(T)$ data were taken in zero applied field whereas the $M/H(T)$ data shown in Fig. 4 were taken in 10 kOe, it is prudent to examine the field dependence of transition associated with T^*. In Fig. 8 we show the $d(MT/H)/dT$ data [36] for the $x = 0.028$ sample for $H \parallel ab = 10$, 30, and 50 kOe. As is commonly seen for antiferromagnetic phase transition, increasing a magnetic field leads to a monotonic suppression of T^*. The inset to Fig. 8 shows that the extrapolated, $H = 0$, T^* value would be 30.7 K as compared to the value of 30.4 K for 10 kOe. This further confirms that there should be (and is) good agreement between the T^* values inferred from 10-kOe magnetization data and the T^* values inferred from the zero-field specific-heat and resistance data in Fig. 7. In addition, these data suggest that magnetic field could be used to fine tune the value of T^*, if needed.

V. SUPERCONDUCTING CRITICAL FIELDS AND ANISOTROPY

Superconductivity can be studied as a function of field (in addition to temperature and doping). Before we present our $H_{c2}(T)$ results, based on $R(T, H)$ data, it is useful to check the $M(H)$ data. We start with $M(H)$ data for $x = 0.024$, $T^* = 29.7$ K, and $T_c = 9.9$ K, taken over a wide field range. The 1.8-K $M(H)$ data shown in Fig. 9 are classically nonlinear, showing a local minimum near $H \sim 2.3$ kOe. For $T = 1.8$ K $< T_c$ the H_{c2} value is clearly higher than the 65-kOe maximum

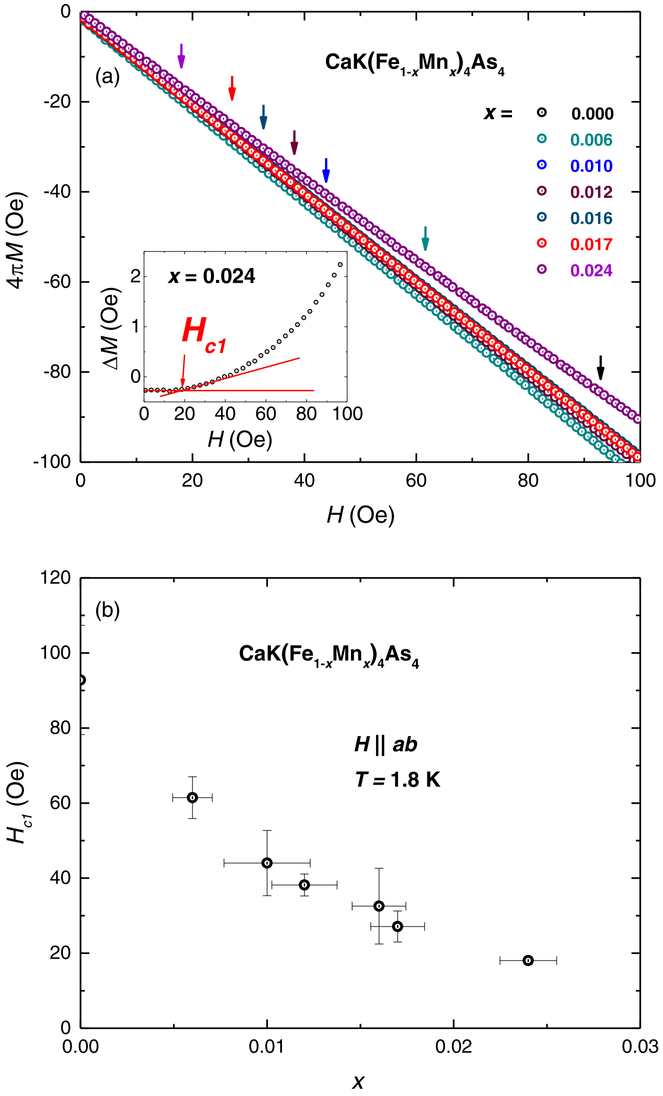

FIG. 10. (a) Magnetization as a function of magnetic field applied parallel to the crystallographic *ab* axis at 1.8 K for different substitution levels. Arrows mark the value of the magnetic field (H_{c1}) where $M(H)$ deviates from linear behavior. Inset shows the criterion we use to determine the H_{c1} values. Remnant field of measurements are smaller than 1 Oe, which is consistent with $M(H)$ plots shown in figure. Temperature is ZFC to 1.8 K and demagnetization is done at 60 K before cooling to minimize the remnant magnetic field (b) H_{c1} value versus x.

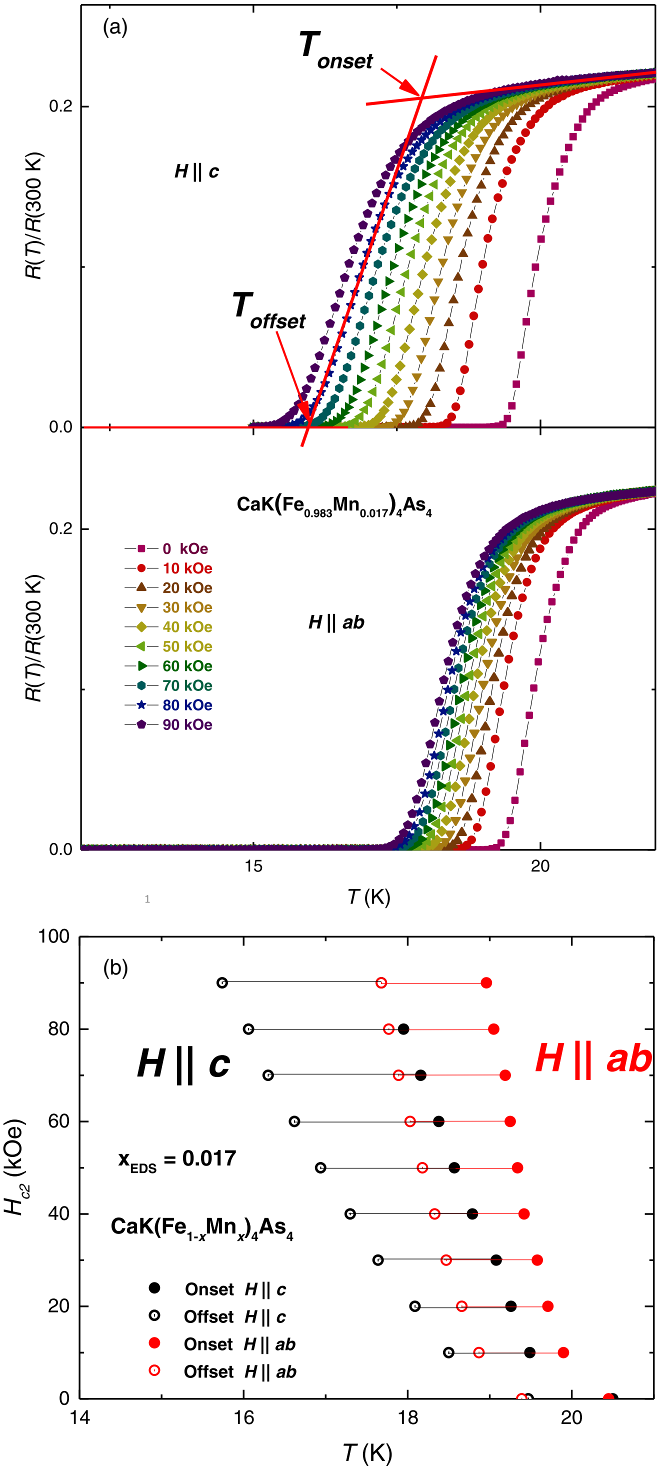

FIG. 11. (a) Temperature-dependent electrical resistance related to the resistance at 300 K in zero field of CaK(Fe$_{0.983}$Mn$_{0.017}$)$_4$As$_4$ single crystal for magnetic field parallel to the crystallographic c axis (upper panel) and ab plane (lower panel) for representative fields $H \leqq 90$ kOe. Onset and offset criteria for T_c are shown by the red solid lines. (b) Anisotropic $H_{c2}(T)$ data determined for two single-crystalline samples of CaK(Fe$_{0.983}$Mn$_{0.017}$)$_4$As$_4$ using onset criterion (solid) and offset criterion (hollow) inferred from the data shown in (a).

field we applied. H_{c1} can be inferred from the lower-field $M(H)$ data.

In order to better estimate H_{c1} values we performed low-field $M(H)$ sweeps at base temperature. In Fig. 10(a) we show the $M(H)$ data for $0 \leqslant x \leqslant 0.024$ for $H \leqslant 100$ Oe. As x increases, the deviation from the fully diamagnetic, linear behavior, that occurs at H_{c1}, appears at lower and lower fields. As shown in inset of Fig. 10(a), ΔM is determined by subtracting the linear, lowest-field behavior of $4\pi M$ from H. Because of the finite thickness of samples, even though magnetic field is applied in ab plane, there is a small demagnetizing factor

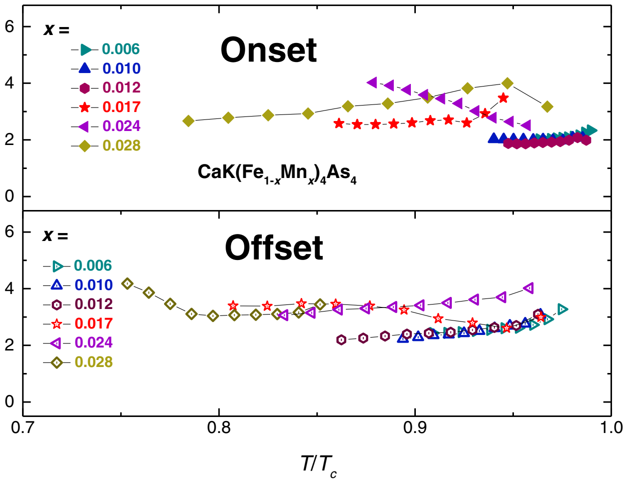

FIG. 12. Anisotropy of the upper critical field $\gamma = H_{c2}^{\parallel ab}(T)/H_{c2}^{\parallel c}(T)$ as a function of effective temperature T/T_c for CaK$(\mathrm{Fe}_{1-x}\mathrm{Mn}_x)_4\mathrm{As}_4$ single crystals, using onset criterion (upper panel) and offset criterion (lower panel), inferred from the temperature-dependent electrical resistance data. The T_c value used to calculate the effective temperature (T/T_c) is the zero-field superconductivity transition temperature for each Mn-substitution level (see Fig. 7 above).

$(n < 0.077)$. Therefore, H_c1 is taken as the vortices start to enter the sample and determined when they deviate from the low field, the nonzero value is due to remnant field of MPMS. The standard error of H_{c1} comes from at least four different samples' measurements. We should note that using this method with higher data density we were able to identify H_{c1} for the pure CaKFe$_4$As$_4$ $(x = 0)$ as ~100 Oe as opposed to the ~1.3-kOe estimated in Ref. [11]. Figure 10(b) shows a monotonic decrease in H_{c1} as Mn substitution increases and T_c decreases.

In order to further study the effects of Mn substitution on the superconducting state, anisotropic $H_{c2}(T)$ data for temperatures near T_c were determined for the substitution levels that have superconductivity. Figure 11(a) shows a representative set of $R(T)/R(300\ \mathrm{K})$ data taken for fixed applied magnetic fields, $H \parallel c$ axis and ab plane $\leqq 90$ kOe for $x = 0.017$. Figure 11(a) also shows an example of the onset and offset criteria used for the evaluation of T_c. Figure 11(b) present the $H_{c2}(T)$ curves for CaK$(\mathrm{Fe}_{0.983}\mathrm{Mn}_{0.017})_4\mathrm{As}_4$ single crystals with both $H \parallel c$ and $H \parallel ab$, showing both the onset (T_{onset}) and offset (T_{offset}) temperatures. For $x = 0.006$, 0.010, 0.012, 0.024, and 0.028, $H_{c2}(T)$ curves are shown in Figs. 24–28. From $H_{c2}(T)$ plots, we can see that T_c is only suppressed by about 3 K when 90-kOe magnetic field is applied, so the complete $H_{c2}(T)$ plots of the CaK$(\mathrm{Fe}_{1-x}\mathrm{Mn}_x)_4\mathrm{As}_4$ compounds cannot be fully determined, however, we still can observe several trends in these data.

Figure 12 shows the temperature-dependent anisotropy ratio $\gamma = H_{c2}^{\parallel ab}(T)/H_{c2}^{\parallel c}(T) \sim 3$ for these samples over the 0.8 $< T/T_c <$ 1.0 range. This value is similar to other 122 and 1144 materials [7,11]. Given that we have determined $H_{c2}(T)$ for temperatures close to T_c, we can evaluate the $H'_{c2}(T)/T_c$ close to T_c, where $H'_{c2}(T)$ is $dH_{c2}(T)/dT$, specifically seeing how it changes as T_c drops below T^* with increasing x. Error of $H'_{c2}(T)/T_c$ comes from linear fit of $H_{c2}(T)$ near the T_c. In the case of other Fe-based systems [37–40] clear changes in $H'_{c2}(T)/T_c$ were associated with changes in the magnetic sublattice coexisting with superconductivity (i.e., ordered or disordered). In Fig. 13 we can see that there is a change in the x dependence of $H'_{c2}(T)/T_c$ for $x > 0.015$, beyond which substitution level suppresses T_c below T^*. Comparison with the slope change of H_{c2} in the pressure-temperature phase diagram of CaK$(\mathrm{Fe}_{1-x}\mathrm{Ni}_x)_4\mathrm{As}_4$ [37] further suggest that this is probably related to changes in the Fermi surface, caused by the onset of the new periodicity associated with the AFM order.

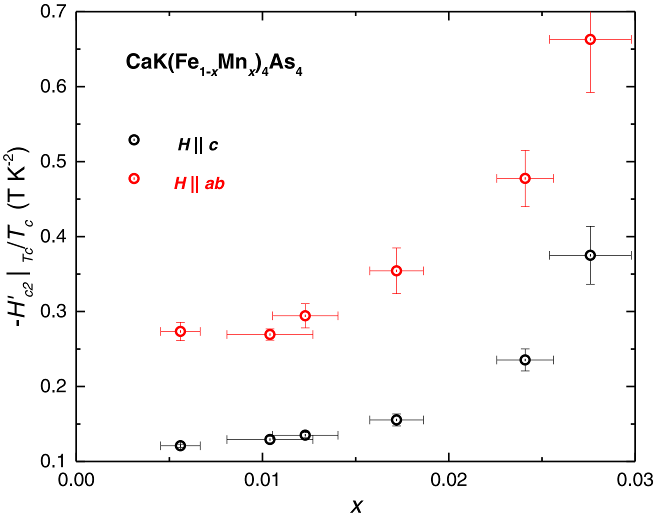

FIG. 13. Substitution dependence of the upper critical field slope $H'_{c2}(T)/T_c$, where $H'_{c2}(T)$ is $dH_{c2}(T)/dT$. T_c is determined by T_{offset} from criteria shown in Fig. 11. Qualitatively similar, albeit somewhat weaker, results can be seen using T_{onset} criterion data.

VI. ELASTORESISTANCE

In order to investigate the evolution of nematic fluctuations in CaK$(\mathrm{Fe}_{1-x}\mathrm{Mn}_x)_4\mathrm{As}_4$ and compare it with Ni-substituted CaKFe$_4$As$_4$ as well as Co-substituted BaFe$_2$As$_2$, we measured elastoresistance. Figure 14 shows the temperature dependence of the elastoresistance coefficients $2m_{66}$ and $m_{11} - m_{12}$ for Mn-1144 samples. These quantities were determined from the strain-induced resistance change $\Delta R/R$ [33] via

$$2m_{66} = (\Delta R/R)_{xx} - (\Delta R/R)_{yy} \tag{1}$$

$$\text{for } \epsilon_{xx}, \epsilon_{yy} \parallel [110]_T, \tag{2}$$

$$m_{11} - m_{12} = (\Delta R/R)_{xx} - (\Delta R/R)_{yy} \tag{3}$$

$$\text{for } \epsilon_{xx}, \epsilon_{yy} \parallel [100]_T. \tag{4}$$

Thus, $2m_{66}$ and $m_{11} - m_{12}$ reflect the elastoresistance coefficients associated with B_{2g} and B_{1g} strain, respectively. For each temperature measured, we found that $(\Delta R/R)_{xx}$ has the opposite sign of $(\Delta R/R)_{yy}$, indicating that the B_{2g}- and B_{1g}-induced resistance changes are much larger than the isotropic A_{1g}-induced strain component [33]. Given that anisotropic strain is the conjugate field to B_{2g} and B_{1g} ne-

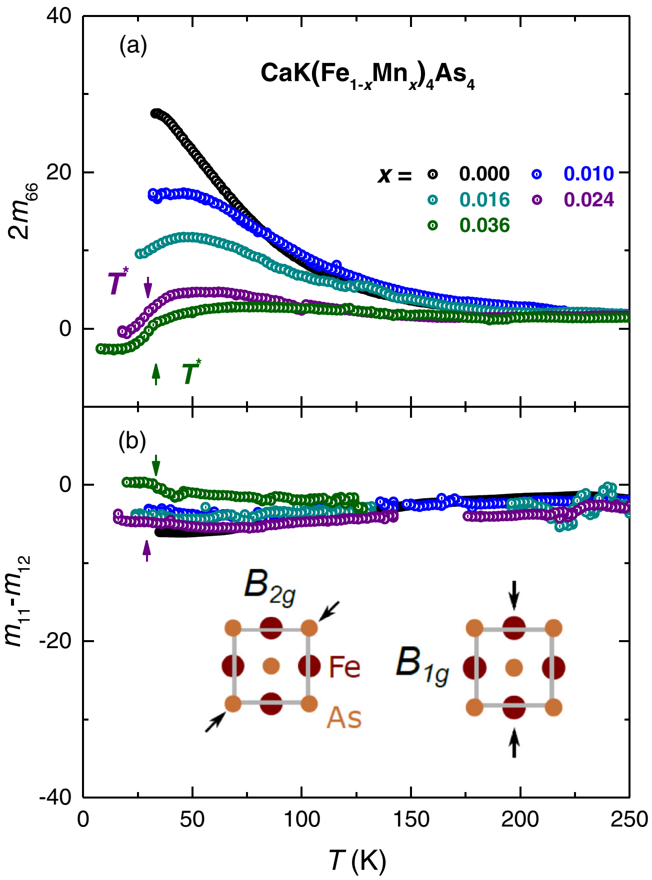

FIG. 14. Elastoresistance coefficients $2m_{66}$ (a) and $m_{11} - m_{12}$ (b) of $\mathrm{CaK(Fe_{1-x}Mn_x)_4As_4}$ for $0 \leqslant x \leqslant 0.036$ as a function of temperature T. Data for $x = 0$ were taken from Ref. [11]. For each x, data were taken down to the superconducting transition temperature T_c. Arrows mark the position of the magnetic transition T^* whenever present, taken from Fig. 7. The insets in (b) visualize the B_{2g} and B_{1g} strains that are experienced by the sample with respect to the FeAs plane.

matic order, the respective elastoresistance coefficients are often considered as a measure of the respective nematic susceptibilites [41]. One should note, however, that the proportionality factor between the elastoresistance coefficients and the nematic susceptibilities $\chi_{\mathrm{nem},i} = k\ m_i$ with $m_i = 2m_{66}$ or $(m_{11} - m_{12})$ does not have to be constant. k can, in principle, be temperature and/or doping dependent, as it depends on microscopic details of the Fermi surface and scattering mechanisms. Nonetheless, the observation of a diverging elastoresistance with Curie-Weiss–type temperature dependence in several Fe-based superconductors, which is in agreement with the theoretical expectations based on a Ginzburg-Landau ansatz and a constant k, can be taken as a good indication that elastoresistance measurements can be used to infer the strength of nematic fluctuations [32,41].

As shown in Fig. 14, $2m_{66}$ of $\mathrm{CaK(Fe_{1-x}Mn_x)_4As_4}$ is characterized by a marked temperature dependence for low x and also changes significantly with doping, whereas $m_{11} - m_{12}$ is only weakly temperature dependent and is essentially doping independent. This suggests that nematic fluctuations, if present, occur only in the B_{2g} channel. A closer look at $2m_{66}$, however, clearly suggests that nematic fluctuations are suppressed with increasing Mn substitution level. In fact, for $x = 0.024$ and 0.036, i.e., those concentrations for which a clear signature of a magnetic transition is observed, the values of $2m_{66}$ across the entire temperature range are comparable to the ones of $m_{11} - m_{12}$. Thus, the magnetic order is very likely not characterized by a nematic component. In other words, a stripe-type magnetic order, as realized in many other pnictides and which would break tetragonal symmetry, can likely be ruled out based on this elastoresistance data. These data suggest that (i) for $\mathrm{CaK(Fe_{1-x}Mn_x)_4As_4}$ the magnetic order may well be a spin-vortex crystal type of antiferromagnetism similar to what was found $\mathrm{CaK(Fe_{1-x}Ni_x)_4As_4}$ [13], and (ii) there may be stripe-type magnetic and nematic fluctuations and susceptibility present in the undoped and weakly doped $\mathrm{CaK(Fe_{1-x}Mn_x)_4As_4}$ but they are suppressed when the doping levels are increased.

Qualitatively, our elastoresistance results for $\mathrm{CaK(Fe_{1-x}Mn_x)_4As_4}$ are similar to the elastoresistance results [42] obtained for the Ni-doped $\mathrm{CaK(Fe_{1-x}Ni_x)_4As_4}$, where Ni substitution stabilizes a spin-vortex crystal magnetic phase [13]. This statement relates to the decrease of $2m_{66}$ with increasing x as well as its complex temperature dependence which does not simply follow Curie-Weiss behavior. Whereas the former is clearly surprising, given that Ni and Mn substitutions lead to a different nominal electron count, the latter might be related to the proportionality factor k between $2m_{66}$ and χ_{nem} not being constant. Another possibility that could give rise to deviations from Curie-Weiss–type behavior is the close proximity of competing magnetically ordered phases, as pointed out from calculations of the nematic susceptibility in a phenomenological model in Ref. [42]. A qualitative difference between the elastoresistance results on Mn- and Ni-substituted $\mathrm{CaKFe_4As_4}$ is the sign of $2m_{66}$ for those x where magnetic order is present. In our experiment, $2m_{66}$ is positive above T_N across the entire range of x studied, whereas for Ni-substituted samples a sign change of $2m_{66}$ from positive to negative was observed for Ni-substitution values that are large enough for the magnetic transition to emerge. It is likely that the differences of the Fermi surface resulting from different electron counts affect the sign of k.

VII. DISCUSSION AND SUMMARY

The T-x phase diagram for $\mathrm{CaK(Fe_{1-x}Mn_x)_4As_4}$ is qualitatively similar to those found for Co- and Ni-substituted $\mathrm{CaKFe_4As_4}$: there is a clear suppression of T_c with increasing Mn substitution as well as an onset of what is likely to be a AFM ordering for $x > 0.015$. For $\mathrm{CaK(Fe_{1-x}Mn_x)_4As_4}$, elastoresistance measurements show that $2m_{66}$ is small compared to the Fe-based superconductors showing stripe-type order. This means that the order is not strongly coupled to an orthorhombic distortion and is analogous to Ni-substituted $\mathrm{CaKFe_4As_4}$, which suggests that AFM structure in Mn-substituted 1144 does not break C_4 symmetry and is still h-SVC.

In Figs. 10 and 13 we presented measurements and analysis of H_{c1} and H_{c2} data. Whereas we do not see any clear effect of the onset of AFM ordering on H_{c1} [Fig. 10(b)], there is a clear effect on H_{c2} (Fig. 13). Using our H_{c1} and H_{c2} data we

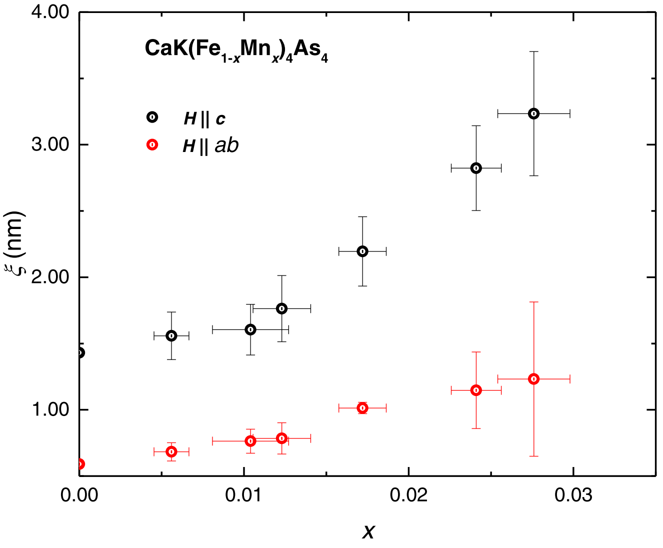

FIG. 15. Coherence length versus x plot of CaK(Fe$_{1-x}$Mn$_x$)$_4$As$_4$ single crystals with applied field in c direction and ab plane.

can extract information about the superconducting coherence length and London penetration depth as well.

Figure 15 shows coherence length ξ of CaK(Fe$_{1-x}$Mn$_x$)$_4$As$_4$ as a function of x. ξ is estimated by using the anisotropic scaling relations $|dH_{c2}^{||c}/dT| = \phi_0/2\pi\xi_\perp^2 T_c$ and $|dH_{c2}^{\perp c}/dT| = \phi_0/2\pi\xi_{||}\xi_\perp T_c$ [11]. Coherence lengths increase as substitution levels increase, and, given that ξ depends on dH_{c2}/dT, it is not surprising that a change in behavior of $\xi(x)$ occurs as the AFM state is entered.

Figure 16(a) shows the London penetration depth λ as a function of x. λ is obtained by using $H_{c1} = \phi_0(\ln\lambda/\xi + 0.5)/(4\pi\lambda^2)$ [43]. Figure 16(b) shows λ^{-2} versus $\sigma\, T_c^2$, where σ is normal-state conductivity which was measured near the T_c. These data roughly follow the behavior associated with Homes-type scaling in the presence of pair breaking [44–46]. Given that there is no clear break in behavior in H_{c1} for $x \sim 0.015$ (Fig. 10), it is not surprising that there is no clear feature in Fig. 16(a) for $x \sim 0.015$.

Figure 17 presents the jump in specific heat at T_c versus T_c for representative 122 systems, as well as for CaK(Fe$_{1-x}$Ni$_x$)$_4$As$_4$ and CaK(Fe$_{1-x}$Mn$_x$)$_4$As$_4$, on a log-log plot [48]; the inset shows just the CaK(Fe$_{1-x}$Ni$_x$)$_4$As$_4$ and CaK(Fe$_{1-x}$Mn$_x$)$_4$As$_4$ data on their own for clarity. The CaK(Fe$_{1-x}$Mn$_x$)$_4$As$_4$ data follow the basic scaling that has been seen for many of the Fe-based superconducting systems, but, at a more quantitative level, the CaK(Fe$_{1-x}$Mn$_x$)$_4$As$_4$ data do fall on or below the lower edge of the manifold, especially when compared to the CaK(Fe$_{1-x}$Ni$_x$)$_4$As$_4$. This would be consistent with the jump in C_p for a given T_c being lower when magnetic pair breaking is present [49,50]. Given that the Mn ions appear to have a relatively large local moment ($\sim$5 μ_B) such magnetic pair breaking could be an additional effect that is not present in the Ni- or Co-doped 1144 or Ni- or Co-doped 122 systems. As mentioned in the Introduction section, since Ba(Fe$_{1-x}$Mn$_x$)$_2$As$_2$ could not stabilize superconductivity, the CaK(Fe$_{1-x}$Mn$_x$)$_4$As$_4$ system is important for assessing the role Mn may play in these Fe-based superconductors.

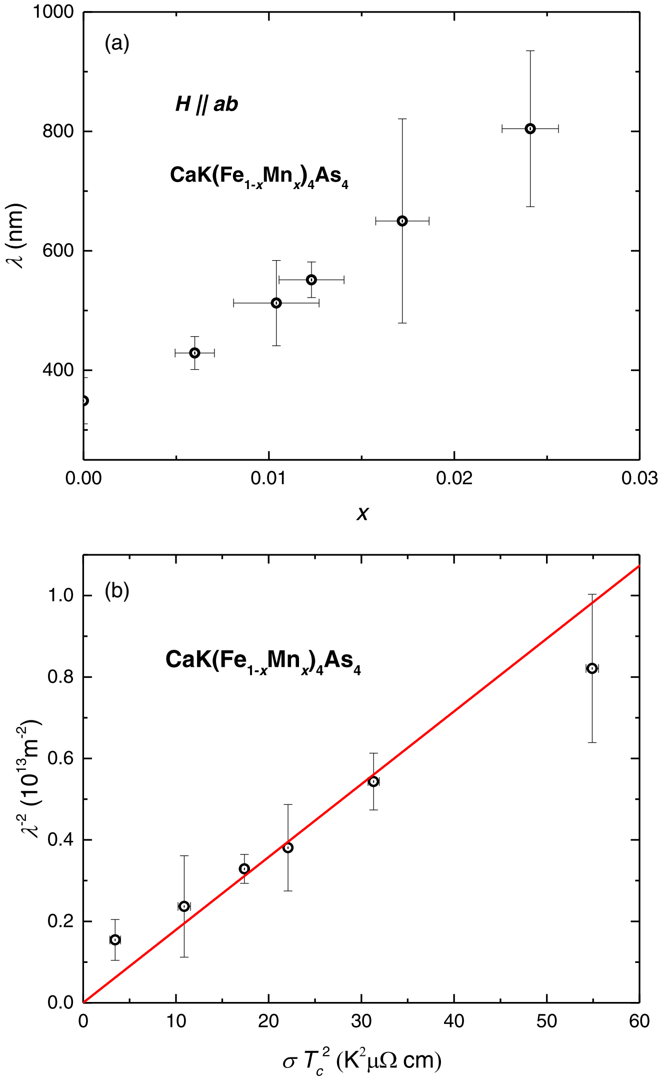

FIG. 16. (a) Shows the London penetration depth as a function of x obtained by magnetic field applied parallel to the crystallographic ab axis with different substitution levels. (b) Shows λ^{-2} versus $\sigma\, T_c^2$. Red line is the linear fit of λ^{-2} versus $\sigma\, T_c^2$ with fixed zero intercept.

For TM = Co and Ni substitutions, the phase diagrams of CaK(Fe$_{1-x}TM_x$)$_4$As$_4$ scaled almost exactly when transition temperatures were plotted not as a function of x, but as a function of band-filling change (i.e., when each Ni atom brings two extra electrons and each Co atom brings only one extra electron) [13,20]. This led to the conclusion that for electron doping of CaKFe$_4$As$_4$ the number of electrons added was the controlling factor for both the stabilization of magnetic ordering as well as for the suppression of superconductivity. In Fig. 18 we show that as Mn is substituted into CaKFe$_4$As$_4$ there is a qualitatively similar suppression of superconductivity as well as the stabilization of magnetic order. This is at odds with the simple analogy that was developed between Co- and Ni-substituted CaKFe$_4$As$_4$ and and (Ba$_{1-x}$K$_x$)Fe$_2$As$_2$. In that analogy CaKFe$_4$As$_4$ could be considered to have the same band filling as Ba$_{0.5}$K$_{0.5}$Fe$_2$As$_2$, giving rise to the expectations that if TM substitution led to rigid band changes in band filling, then (i) Co/Ni doping would suppress superconductivity

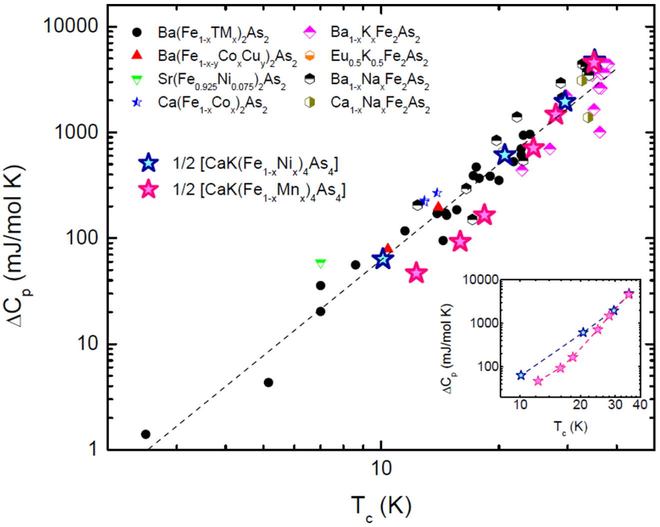

FIG. 17. Scaling of ΔC_p and T_c for 122 and 1144 systems. Figure modified from [47]. For consistency, half of the molecular weight of the 1144 samples was taken for this plot.

and stabilize antiferromagnetic ordering (which does happen) and (ii) Mn doping would lead to a suppression of superconductivity, but not lead to any further magnetic ordering. So, the appearance of clear magnetic ordering in very slightly Mn-substituted CaKFe$_4$As$_4$ is noteworthy.

More quantitatively, in Fig. 18 the CaK(Fe$_{1-x}TM_x$)$_4$As$_4$ phase diagrams for TM = Mn, Co, and Ni are plotted on the same T and $|\Delta e^-|$ axes. This figure shows that whereas the T^* phase lines do overlap, suggesting that the change electron count (positive or negative) can be correlated to the stabilization of magnetic order, the suppression of T_c is much more rapid for Mn substitution than for Ni or Co. Indeed, an unrealistic factor of 4 would be needed to bring the T_c line into agreement with the Co and Ni data.

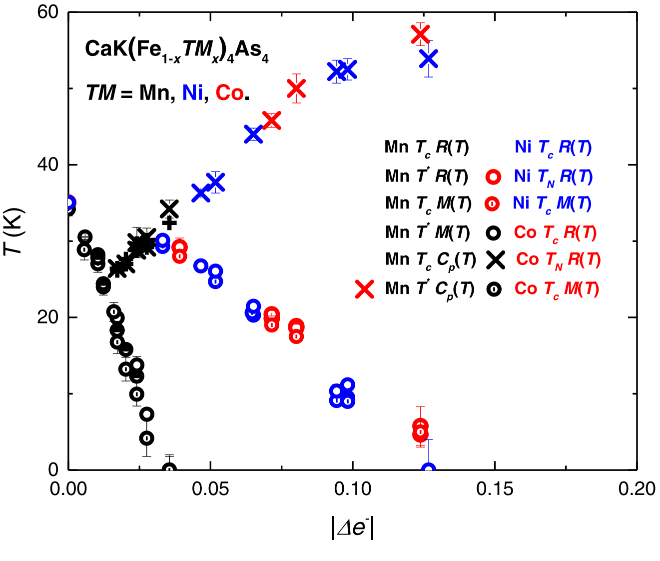

FIG. 18. Temperature vs $|\Delta e^-|$ change of electrons phase diagram of CaK(Fe$_{1-x}TM_x$)$_4$As$_4$ single crystals. TM = Mn, Ni, and Co. The circular symbols denote the T_c phase transitions and the crosslike symbols denote the T^* and T_N phase transitions, which are obtained from resistance, magnetic moment, and specific-heat measurements, denoted as $R(T)$, $M(T)$, and $C_p(T)$.

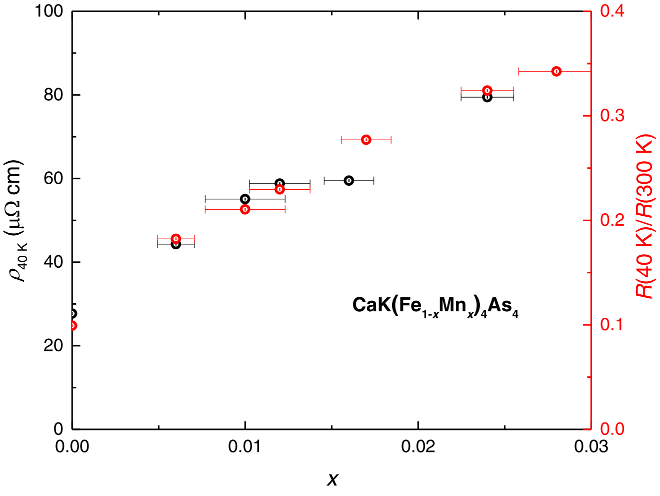

FIG. 19. Resistivity of CaK(Fe$_{1-x}$Mn$_x$)$_4$As$_4$ single crystals at 40 K as the function of Mn-substitution level x (left axes) and R(40 K)/R(300 K) versus x (right axes).

Two possible explanations for the different suppression of T_c readily come to mind. First is the simple acknowledgment that for CaKFe$_4$As$_4$ electron and hole doping via 3d transition metal substitution for Fe may simply have different effects, most likely associated with asymmetries of the density of states of CaKFe$_4$As$_4$ on either side of E_F. The second explanation is given by Abrikosov-Gor'kov mechanism [51] which invokes the large, local moment behavior of the Mn ions and try to understand the enhanced suppression of T_c as being associated with additional breaking of Cooper pairs by spin-flip scattering of electrons off of the local moment Mn impurity (such enhanced Mn pair breaking was already suggested in [23] for Mn substitution into Ba$_{0.5}$K$_{0.5}$Fe$_2$As$_2$). This latter case is intriguing, but would require a rather curious type of high-T_c superconductivity that is both built out of transition metal antiferromagnetic fluctuations and yet is aggressively suppressed by transition metal based magnetic impurities. This apparent contradiction could be reconciled by the fact that the Fe moments that are providing the fluctuations are of order 0.5 μ_B whereas the Mn moments are estimated to be an order of magnitude larger, ~5 μ_B. In this sense, Mn would be acting more like a rare-earth impurity akin to Gd. It should be noted, though, that neither of these possible explanations for the different suppression of T_c help explain or rationalize the fact that T^* lines for Mn, Co, and Ni substitutions do seem to overlap.

In summary, we have been able to grow and study the CaK(Fe$_{1-x}$Mn$_x$)$_4$As$_4$ system. We have been able to assemble a T-x phase diagram that clearly shows the suppression of the superconducting T_c with the addition of Mn, with T_c dropping from 35 K for $x = 0$ to zero for $x > 0.036$, as well as the stabilization of magnetic order for $x > 0.015$, with 26 K $\leqslant T^* \leqslant$ 32 K. The similarity between the T-x phase diagrams for Mn, Co, and Ni substitution, as well as the elastoresistivity data showing no strong indications of a nematic phase transition or fluctuations, strongly suggest that the magnetic

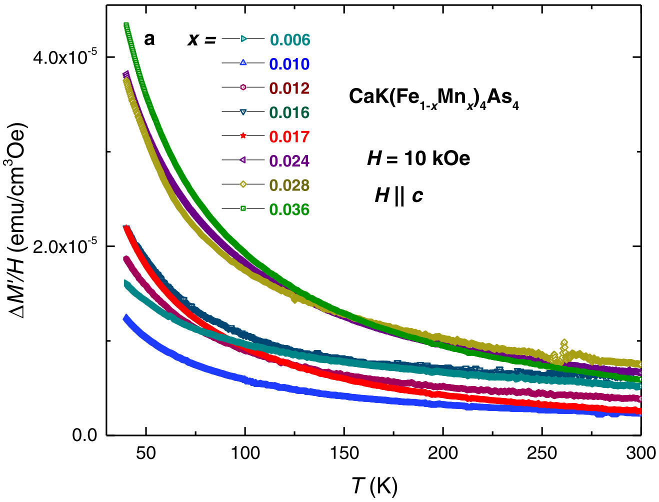

FIG. 20. Difference in the magnetization ($\Delta M'$) between $CaKFe_4As_4$ and $CaK(Fe_{1-x}Mn_x)_4As_4$ single crystals as a function of temperature from 40 to 300 K for a field of 10 kOe applied parallel to the crystallographic *ab* plane shows appearance of Curie-Weiss tail.

ordering associated with T^* is a hedgehog vortex crystal. As x becomes greater than 0.015 and T_c becomes less than T^*, a clear change in the behavior of $H'_{c2}(T)/T_c$ and the associated superconducting coherence length ξ can be seen. These are associated with the probable changes in the Fermi surface that accompanies the AFM ordering at T^*. Comparable features in H_{c1} or the London penetration depth are not clearly resolvable.

The T-x phase diagram for $CaK(Fe_{1-x}Mn_x)_4As_4$ is qualitatively similar to what was found for Ni- and Co-1144 including the appearance of Mn-stabilized antiferromagnetic ordering. Whereas the stabilization of antiferromagnetic ordering occurs at the same rate (per change in band filling) as it does for Ni or Co substitutions, the suppression of T_c is much faster (by a factor of roughly 4). The ΔC_p versus T_c plot for $CaK(Fe_{1-x}Mn_x)_4As_4$ also drops somewhat faster than would be expected when compared to the $CaK(Fe_{1-x}Ni_x)_4As_4$ data. Both of these enhanced suppressions may be associated with

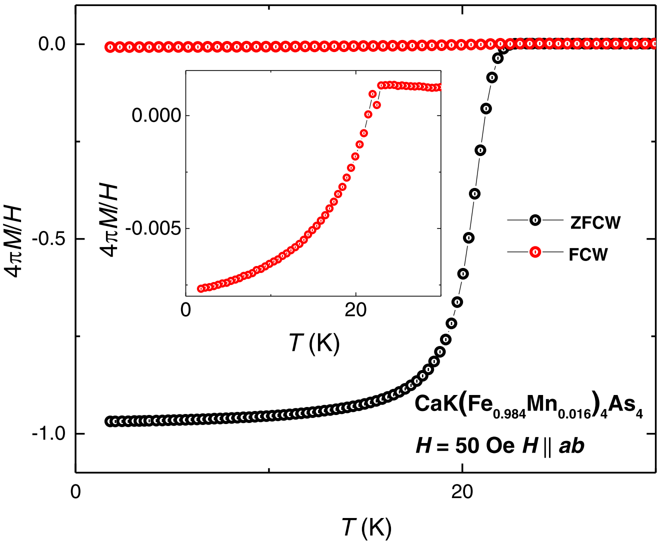

FIG. 21. Zero-field-cooled-warming (ZFCW) and field-cooled (FCW) low-temperature magnetization as a function of temperature for $CaK(Fe_{0.984}Mn_{0.016})_4As_4$ single crystals with a field of 50 Oe applied parallel to the crystallographic *ab* plane. M is the volumetric magnetic moment with cgs unit emu cm^{-3} or Oe.

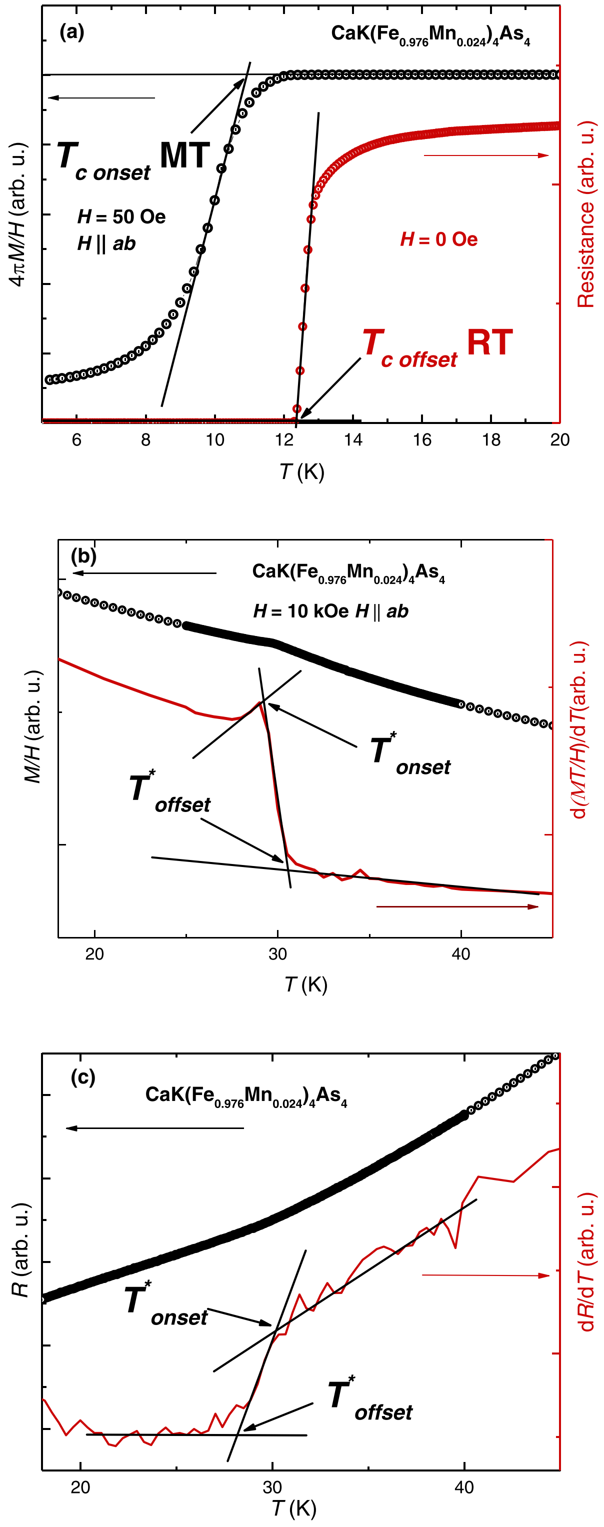

FIG. 22. Onset and offset criteria for T_c (a) and T^* (b), (c) based on magnetization and resistance measurement.

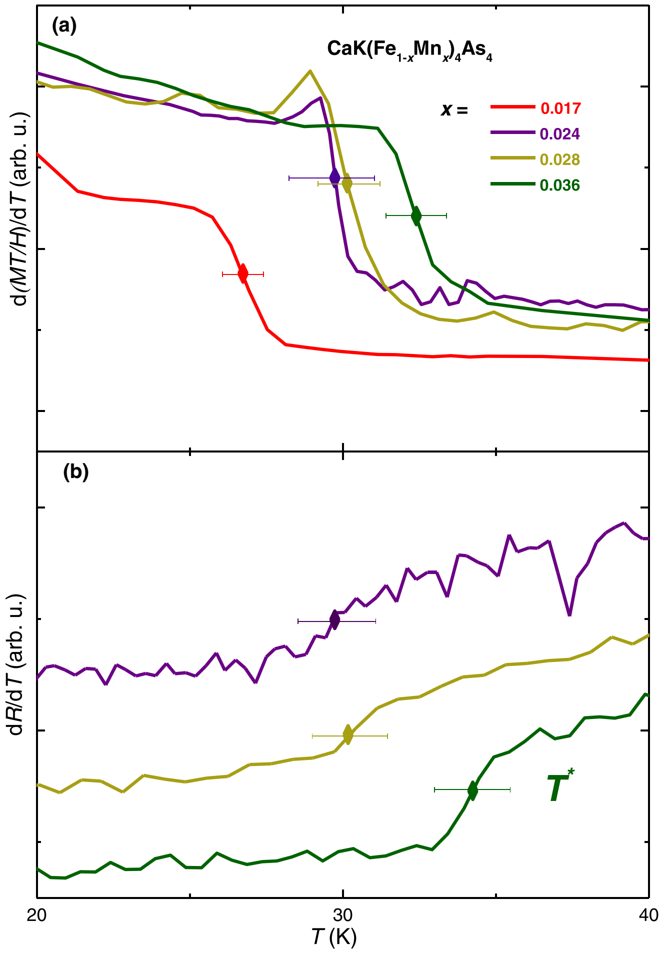

FIG. 23. The T^* anomaly appears clearly as a step in both plot $d(MT/H)dT$ (a) and the derivative of resistance dR/dT (b). Only the data above T_c are plotted.

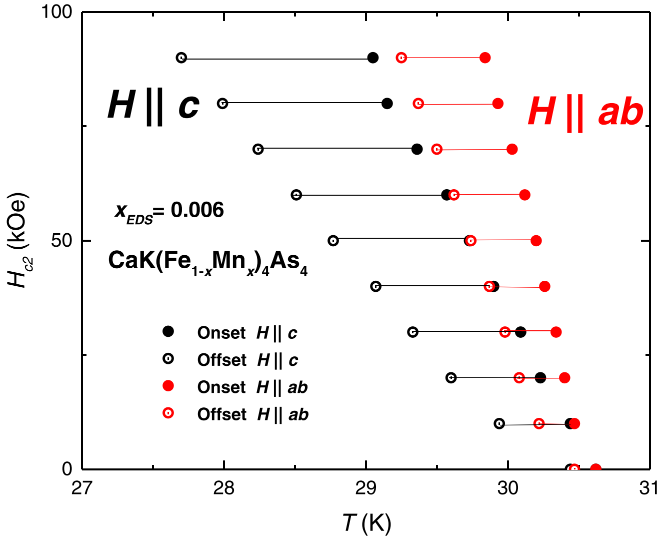

FIG. 24. Anisotropic $H_{c2}(T)$ data determined for two single-crystalline samples of $x_{\mathrm{EDS}} = 0.006$ CaK$(\mathrm{Fe}_{1-x}\mathrm{Mn}_x)_4\mathrm{As}_4$ using onset criterion (solid) and offset criterion (hollow) inferred from the temperature-dependent electrical resistance data.

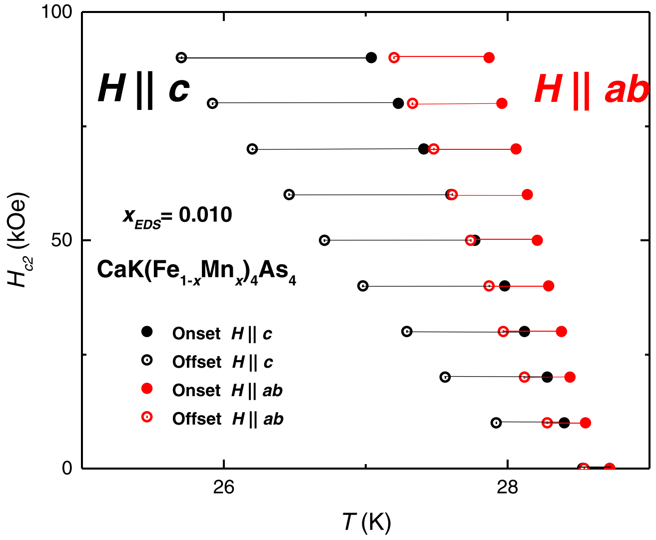

FIG. 25. Anisotropic $H_{c2}(T)$ data determined for two single-crystalline samples of $x_{\mathrm{EDS}} = 0.010$ CaK$(\mathrm{Fe}_{1-x}\mathrm{Mn}_x)_4\mathrm{As}_4$ using onset criterion (solid) and offset criterion (hollow) inferred from the temperature-dependent electrical resistance data.

the large effective moment found for the substituted Mn ions, ~5 μ_B, as compared to the size of the ordered Fe moments (~0.5 μ_B).

ACKNOWLEDGMENTS

We thank A. Kreyssig and B. Kuthanazhi for useful discussions. We would like to thank E. F. Talantsev for pointing to a units conversion error in the initial version of the paper. Work at the Ames Laboratory was supported by the U.S. Department of Energy, Office of Science, Basic Energy Sciences, Materials Sciences and Engineering Division. The Ames Laboratory is operated for the U.S. Department of Energy by Iowa

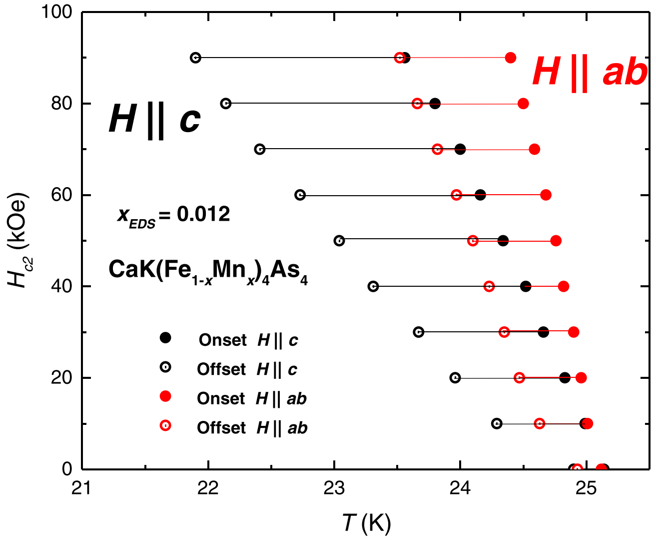

FIG. 26. Anisotropic $H_{c2}(T)$ data determined for two single-crystalline samples of $x_{\mathrm{EDS}} = 0.012$ CaK$(\mathrm{Fe}_{1-x}\mathrm{Mn}_x)_4\mathrm{As}_4$ using onset criterion (solid) and offset criterion (hollow) inferred from the temperature-dependent electrical resistance data.

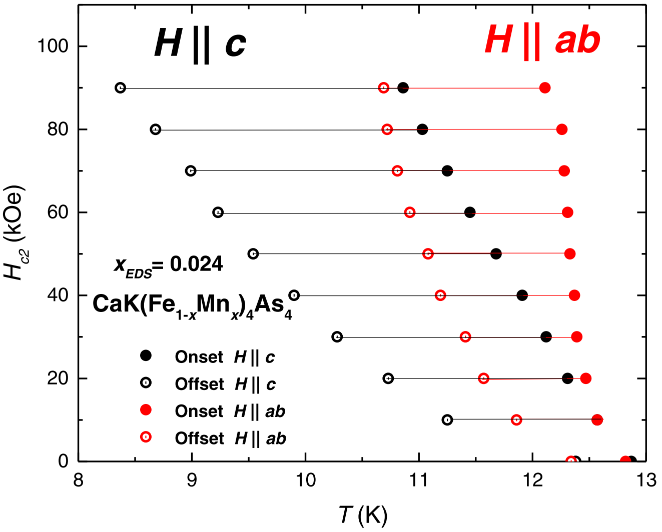

FIG. 27. Anisotropic $H_{c2}(T)$ data determined for two single-crystalline samples of $x_{\mathrm{EDS}} = 0.024$ CaK(Fe$_{1-x}$Mn$_x$)$_4$As$_4$ using onset criterion (solid) and offset criterion (hollow) inferred from the temperature-dependent electrical resistance data.

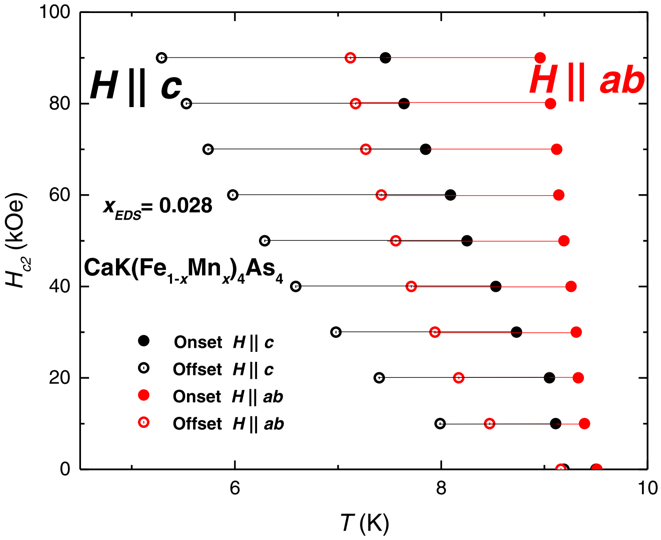

FIG. 28. Anisotropic $H_{c2}(T)$ data determined for two single-crystalline samples of $x_{\mathrm{EDS}} = 0.028$ CaK(Fe$_{1-x}$Mn$_x$)$_4$As$_4$ using onset criterion (solid) and offset criterion (hollow) inferred from the temperature-dependent electrical resistance data.

State University under Contract No. DE-AC02-07CH11358. E.G. and W.R.M. were supported, in part, by the Gordon and Betty Moore Foundations EPiQS Initiative through Grant No. GBMF4411. L.X. was supported by the W. M. Keck Foundation.

APPENDIX

Figure 19 shows resistivity ρ for $T = 40$ K of CaK(Fe$_{1-x}$Mn$_x$)$_4$As$_4$ single crystals as the function of x. Error of resistivity is less estimated due to the measurement difficult of thickness. On the right-hand axes of Fig. 19 we plot the related quantity $R(40\ \mathrm{K})/R(300\ \mathrm{K})$ versus x. The value of resistivity becomes larger as increasing of x, which indicates increased disorder scattering due to substitution.

Figure 20 shows the difference in the magnetization ($\Delta M'$) between CaK(Fe$_{1-x}$Mn$_x$)$_4$As$_4$ and CaKFe$_4$As$_4$ single crystals as a function of temperature from 40 to 300 K with a field of 10 kOe applied parallel to the crystallographic *ab* plane. The magnetization plots have the appearance of Curie-Weiss tails suggesting that the Mn-substituted system has local moment behavior. In order to determine if these are indeed Curie-Weiss tails, fitting was done by assuming that local moment behavior is only due to Mn and fixing θ values to be determined by T^* value or its extrapolation by linear fitting T^* to $x = 0.006$ for low x, where T^* is absent to $x = 0.006$ for low x, where T^* is absent. Due to the small signals in the high-temperature range, we performed fitting from 40 to 200 K. Table I shows the result of fitting. The value of μ_{eff} is around 5 μ_B and R^2 (COD) values are larger than 0.99. R (COD) is also known as coefficient of determination which is a statistical measure to qualify the linear regression. If R^2 is 1, it indicates that the fitted line explains all the variability of the response data around its mean [52]. The fitting results strongly suggest that Mn, unlike Ni or Co in CaK(Fe$_{1-x}TM_x$)$_4$As$_4$, [20] is more local-like-moment bearing.

Figure 21 shows zero-field-cooled-warming (ZFCW) and field-cooled-warming (FCW) low-temperature magnetization as a function of temperature for CaK(Fe$_{0.984}$Mn$_{0.016}$)$_4$As$_4$ single crystals with a field of 50 Oe applied parallel to *ab* plane. The large difference between ZFCW and FCW is consistent with the large pinning found even in CaKFe$_4$As$_4$ [53].

Criteria for inferring T_c and T^* are shown in Fig. 22. For T_c [Fig. 22(a)] we use an onset criterion for our $M(T)$ data and an offset criterion for our $R(T)$ data. As is often the case, these criteria agree well, especially in the low-field limit. For T^*, although the feature is much clearer for Mn substitution than it was for Ni or Co substitution [20], the features in $M(T)$ and $R(T)$ are still somewhat subtle. In order to infer T^*, we take the average of onset and offset values and use the difference as error.

$dR(T)/dT$ and $dM(T)/dT$ data for several different x values are shown in Fig. 23, showing good agreement between the position of the T^* features.

Figures 24–28 present $H_{c2}(T)$ curves which are obtained from $R(T)$ data for fixed applied fields and the criteria shown in Fig. 11(a) of CaK(Fe$_{1-x}$Mn$_x$)$_4$As$_4$ single crystals for $x =$ 0.006, 0.010, 0.012, 0.024, and 0.028.

---

[1] Y. Kamihara, T. Watanabe, M. Hirano, and H. Hosono, J. Am. Chem. Soc. **130**, 3296 (2008).
[2] D. C. Johnston, Adv. Phys. **59**, 803 (2010).
[3] J. Paglione and R. L. Greene, Nat. Phys. **6**, 645 (2010).
[4] H. Hosono and K. Kuroki, Phys. C (Amsterdam) **514**, 399 (2015).
[5] P. C. Canfield, S. L. Bud'ko, N. Ni, J. Q. Yan, and A. Kracher, Phys. Rev. B **80**, 060501(R) (2009).

[6] N. Ni, A. Thaler, A. Kracher, J. Q. Yan, S. L. Bud'ko, and P. C. Canfield, Phys. Rev. B **80**, 024511(R) (2009).

[7] N. Ni, A. Thaler, J. Q. Yan, A. Kracher, E. Colombier, S. L. Bud'ko, P. C. Canfield, and S. T. Hannahs, Phys. Rev. B **82**, 024519(R) (2010).

[8] P. C. Canfield and S. L. Bud'ko, Annu. Rev. Condens. Matter Phys. **1**, 27 (2010).

[9] G. R. Stewart, Rev. Mod. Phys. **83**, 1589 (2011).

[10] A. Iyo, K. Kawashima, T. Kinjo, T. Nishio, S. Ishida, H. Fujihisa, Y. Gotoh, K. Kihou, H. Eisaki, and Y. Yoshida, J. Am. Chem. Soc. **138**, 3410 (2016).

[11] W. R. Meier, T. Kong, U. S. Kaluarachchi, V. Taufour, N. H. Jo, G. Drachuck, A. E. Böhmer, S. M. Saunders, A. Sapkota, A. Kreyssig, M.A. Tanatar, R. Prozorov, A. I. Goldman, F. F. Balakirev, A. Gurevich, S. L. Budko, and P. C. Canfield, Phys. Rev. B **94**, 064501(R) (2016).

[12] W. R. Meier, T. Kong, S. L. Bud'ko, and P. C. Canfield, Phys. Rev. Materials **1**, 013401 (2017).

[13] W. R. Meier, Q.-P. Ding, A. Kreyssig, S. L. Bud'ko, A. Sapkota, K. Kothapalli, V. Borisov, R. Valentí, C. D. Batista, P. P. Orth *et al.*, npj Quantum Mater. **3**, 5 (2018).

[14] F.-C. Hsu, J.-Y. Luo, K.-W. Yeh, T.-K. Chen, T.-W. Huang, P. M. Wu, Y.-C. Lee, Y.-L. Huang, Y.-Y. Chu, D.-C. Yan *et al.*, Proc. Natl. Acad. Sci. USA **105**, 14262 (2008).

[15] A. E. Böhmer and A. Kreisel, J. Phys.: Condens. Matter **30**, 23001 (2018).

[16] K. Kawashima, T. Kinjo, T. Nishio, S. Ishida, H. Fujihisa, Y. Gotoh, K. Kihou, H. Eisaki, Y. Yoshida, and A. Iyo, J. Phys. Soc. Jpn. **85**, 64710 (2016).

[17] J.-K. Bao, K. Willa, M. P. Smylie, H. Chen, U. Welp, D. Y. Chung, and M. G. Kanatzidis, Cryst. Growth Des. **18**, 3517 (2018).

[18] E. Gati, L. Xiang, S. L. Bud'ko, and P. C. Canfield, Ann. Phys. **532**, 2000248 (2020).

[19] I. I. Mazin, Nature (London) **464**, 183 (2010).

[20] W. Meier, thesis, https://lib.dr.iastate.edu/etd/16856/.

[21] K. Iida, Y. Nagai, S. Ishida, M. Ishikado, N. Murai, A. D. Christianson, H. Yoshida, Y. Inamura, H. Nakamura, A. Nakao, K. Munakata, D. Kagerbauer, M. Eisterer, K. Kawashima, Y. Yoshida, H. Eisaki, and A. Iyo, Phys. Rev. B **100**, 014506(R) (2019).

[22] D. Collomb, S. J. Bending, A. E. Koshelev, M. P. Smylie, L. Farrar, J.-K. Bao, D. Y. Chung, M. G. Kanatzidis, W.-K. Kwok, and U. Welp, Phys. Rev. Lett. **126**, 157001(R) (2021).

[23] J. Li, Y. F. Guo, S. B. Zhang, J. Yuan, Y. Tsujimoto, X. Wang, C. I. Sathish, Y. Sun, S. Yu, W. Yi, K. Yamaura, E. Takayama-Muromachiu, Y. Shirako, M. Akaogi, and H. Kontani, Phys. Rev. B **85**, 214509(R) (2012).

[24] D. LeBoeuf, Y. Texier, M. Boselli, A. Forget, D. Colson, and J. Bobroff, Phys. Rev. B **89**, 035114(R) (2014).

[25] A. Thaler, H. Hodovanets, M. S. Torikachvili, S. Ran, A. Kracher, W. Straszheim, J. Q. Yan, E. Mun, and P. C. Canfield, Phys. Rev. B **84**, 144528(R) (2011).

[26] A. Pandey, V. K. Anand, and D. C. Johnston, Phys. Rev. B **84**, 014405(R) (2011).

[27] P. C. Canfield, Rep. Prog. Phys. **83**, 16501 (2020).

[28] P. C. Canfield, T. Kong, U. S. Kaluarachchi, and N. H. Jo, Philos. Mag. **96**, 84 (2016).

[29] A. Jesche, M. Fix, A. Kreyssig, W. R. Meier, and P. C. Canfield, Philos. Mag. **96**, 2115 (2016).

[30] D. E. Newbury and N. W. M. Ritchie, in *Scanning Microscopies 2014*, edited by M. T. Postek, D. E. Newbury, S. F. Platek, and T. K. Maugel (SPIE, Bellingham, WA, 2014), Vol. 9236, p. 92360H.

[31] R. Prozorov and V. G. Kogan, Phys. Rev. Applied **10**, 014030 (2018).

[32] H.-H. Kuo, J.-H. Chu, J. C. Palmstrom, S. A. Kivelson, and I. R. Fisher, Science **352**, 958 (2016).

[33] H.-H. Kuo, M. C. Shapiro, S. C. Riggs, and I. R. Fisher, Phys. Rev. B **88**, 085113(R) (2013).

[34] Y. Liu, Y.-B. Liu, Y.-L. Yu, Q. Tao, C.-M. Feng, and G.-H. Cao, Phys. Rev. B **96**, 224510(R) (2017).

[35] Y.-B. Liu, Y. Liu, Y.-W. Cui, Z. Ren, and G.-H. Cao, J. Phys.: Condens. Matter **32**, 175701 (2020).

[36] M. E. Fisher, Philos. Mag. **7**, 1731 (1962).

[37] L. Xiang, W. R. Meier, M. Xu, U. S. Kaluarachchi, S. L. Bud'ko, and P. C. Canfield, Phys. Rev. B **97**, 174517(R) (2018).

[38] U. S. Kaluarachchi, V. Taufour, A. E. Böhmer, M. A. Tanatar, S. L. Bud'ko, V. G. Kogan, R. Prozorov, and P. C. Canfield, Phys. Rev. B **93**, 064503(R) (2016).

[39] L. Xiang, U. S. Kaluarachchi, A. E. Böhmer, V. Taufour, M. A. Tanatar, R. Prozorov, S. L. Bud'ko, and P. C. Canfield, Phys. Rev. B **96**, 024511(R) (2017).

[40] V. Taufour, N. Foroozani, M. A. Tanatar, J. Lim, U. Kaluarachchi, S. K. Kim, Y. Liu, T. A. Lograsso, V. G. Kogan, R. Prozorov, S. L. Budko, J. S. Schilling, and P. C. Canfield, Phys. Rev. B **89**, 220509(R) (2014).

[41] J.-H. Chu, H.-H. Kuo, J. G. Analytis, and I. R. Fisher, Science **337**, 710 (2012).

[42] A. E. Böhmer, F. Chen, W. R. Meier, M. Xu, G. Drachuck, M. Merz, P. W. Wiecki, S. L. Bud'ko, V. Borisov, R. Valentí *et al.*, arXiv:2011.13207.

[43] K. Cho, A. Fente, S. Teknowijoyo, M. A. Tanatar, K. R. Joshi, N. M. Nusran, T. Kong, W. R. Meier, U. Kaluarachchi, I. Guillamón, H. Suderow, S. L. Budko, P. C. Canfield, and R. Prozorov, Phys. Rev. B **95**, 100502(R) (2017).

[44] S. V. Dordevic, D. N. Basov, and C. C. Homes, Sci. Rep. **3**, 1713 (2013).

[45] V. G. Kogan, Phys. Rev. B **87**, 220507(R) (2013).

[46] V. G. Kogan, R. Prozorov, and V. Mishra, Phys. Rev. B **88**, 224508(R) (2013).

[47] S. L. Bud'ko, V. G. Kogan, R. Prozorov, W. R. Meier, M. Xu, and P. C. Canfield, Phys. Rev. B **98**, 144520(R) (2018).

[48] S. L. Bud'ko, N. Ni, and P. C. Canfield, Phys. Rev. B **79**, 220516(R) (2009).

[49] S. Skalski, O. Betbeder-Matibet, and P. R. Weiss, Phys. Rev. **136**, A1500 (1964).

[50] S. L. Bud'ko, V. G. Kogan, H. Hodovanets, S. Ran, S. A. Moser, M. J. Lampe, and P. C. Canfield, Phys. Rev. B **82**, 174513(R) (2010).

[51] A. A. Abrikosov and L. P. Gor'kov, Zh. Eksp. Teor. Fiz. **39**, 1781 (1960) [Sov. Phys. JETP **12**, 1243 (1961)].

[52] OriginLab, Origin Help, https://www.originlab.com/doc/Origin-Help/Interpret-Regression-Result#R-Square_.28COD.29.

[53] Y. Tomioka, M. Naito, and K. Kitazawa, Phys. C (Amsterdam) **215**, 297 (1993).